nature communications

Article

https://doi.org/10.1038/s41467-025-64734-y

The integral membrane protein smim4 modulates redox balance via malate compartmentalization in pancreatic cancer

Received: 25 September 2024

Accepted: 23 September 2025

Published online: 05 November 2025

Check for updates

Bo Wang[1,10], Xinyu Han[2,3,10], Xianlong Lin[3,10], Jinjing Wang[3,10], Chang You[3], Keke Chen[3], Yu Chen[3], Fanhao Meng[3], Huihui Jiang[3], Fulong Zheng[3], Yiqing Zhang[3], Jinya Lyu[3], Yuxiao Bai[4], Xiaoning Qu[4], Danyi Zhou[3], Minghua Jiang[4] ✉, Wei Cui[5] ✉, Jianxin Lyu[1,6] ✉ & Hezhi Fang[7,8,9] ✉

Reshaping metabolic compartmentalization is frequently observed in cancer cells, however, the underlying mechanisms and physiological implications are less known. Here, we show that pancreatic ductal adenocarcinoma (PDAC) patients with low integral membrane protein SMIM4 expression exhibits a poor prognosis and reduces oxidative stress in tumors, which can be confirmed in cultured human PDAC cells and mice *Pdx1-Cre/Kras*$^{G12D/+}$*/Trp53R*$^{172H/+}$ (KPC) cells. Mechanistically, SMIM4 interacts with and facilitates the assembly of SLC25A1-containing complexes, enabling SLC25A1-mediated malate/citrate exchange. Depleting *SMIM4* has little effect on mitochondrial respiration but impairs the assembly of SLC25A1-containing complexes, thereby reshaping of malate compartmentalization. This shift promotes NADPH generation through increased cytosolic conversion of malate to pyruvate, protecting cells from glucose deprivation-induced apoptosis. Moreover, PDAC cells with low level of SMIM4 are resistant to RSL3-induced toxicity, indicating that PDAC tumors with high SMIM4 expression are promising candidates for treatment with oxidative stress inducers.

Pancreatic ductal adenocarcinoma (PDAC) is a lethal disease and has the lowest 5-year survival rate among all cancer types[1]. Although PDAC tumors are hypovascular and the cancer cells are surrounded by condensed stromal cells[2], the influx of metabolic substrates from the circulation into the tumor microenvironment (TME) is limited[3]. To overcome this inadequate nutrient supply[4,5], PDAC cells undergo metabolic reprogramming to support their proliferation. Tumor ductal cells with limited supplies of glucose and/or glutamine can use

[1]Department of Clinical Laboratory, The Second Affiliated Hospital and Yuying Children's Hospital of Wenzhou Medical University; School of Laboratory Medicine and Life Sciences, Wenzhou Medical University, Wenzhou, Zhejiang, China. [2]Department of Clinical Laboratory, Zhangzhou Affiliated Hospital of Fujian Medical University, Zhangzhou, China. [3]College of Laboratory Medicine and Life Sciences, Wenzhou Medical University, Wenzhou, Zhejiang, China. [4]Department of Clinical Laboratory, The Second Affiliated Hospital and Yuying Children's Hospital of Wenzhou Medical University, Wenzhou, Zhejiang, China. [5]Department of Clinical Laboratory, State Key Laboratory of Molecular Oncology, National Cancer Center/National Clinical Research Center for Cancer/Cancer Hospital, Chinese Academy of Medical Sciences and Peking Union Medical College, Beijing, China. [6]Laboratory Medicine Center, Department of Clinical Laboratory, Zhejiang Provincial People's Hospital, Affiliated People's Hospital, Hangzhou Medical College, Hangzhou, Zhejiang, China. [7]Department of Anesthesia and Critical Care, The Second Affiliated Hospital and Yuying Children's Hospital of Wenzhou Medical University; Key Laboratory of Pediatric Anesthesiology, Ministry of Education, Wenzhou Medical University, Wenzhou, Zhejiang, China. [8]Department of Clinical Laboratory, National Cancer Center/National Clinical Research Center for Cancer/Cancer Hospital, Chinese Academy of Medical Sciences and Peking Union Medical College, Beijing, China. [9]Zhejiang Provincial Key Laboratory of Medical Genetics, School of Laboratory Medicine and Life Sciences, Wenzhou Medical University, Wenzhou, Zhejiang, China. [10]These authors contributed equally: Bo Wang, Xinyu Han, Xianlong Lin, Jinjing Wang. ✉e-mail: minghua93@126.com; cui123@cicams.ac.cn; jxlu313@163.com; fangh@wmu.edu.cn; fangh@cicams.ac.cn

extracellular proteins as a biosynthetic resource via micropinocytosis in a KRAS-dependent manner[4,6]. Furthermore, alternative biosynthetic metabolites for PDAC cell proliferation in nutrient-deficient conditions include serine[7], alanine[8], lipids[9], and nucleotides[10,11]. Understanding the regulatory mechanisms of the metabolism of extracellular metabolites can aid the development of treatments for PDAC[12,13]. However, given the negligible antioxidative properties of these extracellular metabolites, how PDAC cells survive oxidative stress within the TME, particularly with insufficient glucose and glutamine levels, remains unclear.

While the Warburg effect proposes that rapidly proliferating cells rely on glycolysis, rather than mitochondrial metabolism, the essentiality of mitochondria in cancer cell metabolism has been overlooked[14]. Until recently, mitochondrial metabolism, particularly respiration-coupled metabolism, was thought to play an indispensable role in the synthesis of nucleotides and proteins in proliferating cells[15–17]. Unsurprisingly, given that the TME of PDAC cells lacks glucose, PDAC cells require increased mitochondrial metabolism for survival[18], growth[19], and metastasis[20].

Cancer cells require nicotinamide adenine dinucleotide phosphate (NADPH), a reducing agent, for both the biosynthesis of macromolecules and regeneration of antioxidant molecules. The survival of cancer cells with limited glucose supplies is challenged by oxidative stress due to the inability of the cells to generate NADPH via the pentose phosphate pathway (PPP). NADPH can also be generated in a mitochondrial-dependent manner, which involves malate to pyruvate conversion via ME1/2, citrate to alpha-ketoglutarate conversion via IDH1/2, and the one-carbon cycle[21]; therefore, mitochondria-mediated NADPH generation is typically enhanced in cancer cells lacking glucose. Thus, targeting mitochondria-associated NADPH generation is a potential therapeutic strategy for the treatment of PDAC[22]. Although KRAS is known to promote mitochondrial metabolism to increase NADPH generation in the cytosol via GOT1[23], the regulatory mechanisms underlying NADPH generation in the mitochondria of PDAC cells under nutrient stress remain largely unknown.

Mitochondria contain approximately 1000–1500 different proteins, but the functions of over 100 of these are poorly understood[24]. Identifying poorly characterized metabolic regulatory proteins or enzymes among these uncharacterized proteins has become a crucial area of interest[25–28], because there are hundreds of hydrophilic metabolites that are transported across metabolic transporters localized on the inner mitochondrial membrane, but the transporters of many mitochondrial metabolites, such as asparagine and formate[29,30], remain unknown. Notably, many uncharacterized mitochondrial metabolite transporters have been pre-allocated to the SLC25A family and SFXNs (sideroflexin carriers)[31]. Exploring the function of poorly characterized metabolite transporters and their regulatory factors has aided our understanding of cell metabolism and its implication on human diseases[32–36]. In this study, we explored the function of small integral membrane protein (SMIM4), a poorly characterized PDAC-associated mitochondrial protein, and identified it as a malate/citrate transporter regulatory protein. Thus, we provided insights into how PDAC cells regulate NADPH generation to survive under nutrient-deficient conditions.

Results

SMIM4 is a mitochondrial protein and favorable prognostic marker of pancreatic cancer

To identify uncharacterized and pancreatic cancer-associated mitochondrial proteins, we reviewed a total of 1121 mitochondria-localized proteins indexed by the Human Protein Atlas (HPA, https://www.proteinatlas.org/, updated in 2021) and found that 257 proteins were poorly characterized (Fig. 1A, **left** and Supplementary Data 1). Transcriptome analysis further revealed that 103 of the 257 genes exhibited significant differential expression between cancerous (The Cancer Genome Atlas [TCGA], https://portal.gdc.cancer.gov/) and normal (Genotype-Tissue Expression [GTEx], https://gtexportal.org/home/) pancreatic tissues (Fig. 1A, **middle panel**), of these 15 genes are prognostic markers of pancreatic cancer at the RNA level (TCGA) (Fig. 1A, right panel), *SMIM4* (medium expression) is a favorable prognostic marker with the lowest hazard ratio (HR < 1) and the strongest significance (Fig. 1B, C and Supplementary Fig. 1A). Moreover, *SMIM4* expression was confirmed as a favorable prognostic marker in another published PDAC cohort ($n = 42$) (Fig. 1D and Supplementary Fig. 1B)[37], and immunohistochemistry (IHC) analysis of Shanghai cohort showed that patients with higher SMIM4 protein levels in their tumor ductal cells exhibited longer survival rates (Fig. 1E and Supplementary Fig. 1C), which was confirmed further in Wenzhou cohort with relatively smaller sample size (Supplementary Fig. 1D). A combined correlation analysis further revealed that metastatic PDAC tumors have lower SMIM4 levels compared to non-metastatic tumors (Fig. 1F). Additionally, the expression of SMIM4 is negatively associated with the clinical PDAC biomarker CA19-9, an increase of which is generally associated with worse disease prognosis (Fig. 1G). All these data together strongly indicated that SMIM4 is a favorable prognostic marker of pancreatic cancer.

While mitochondrial localization of SMIM4 was not fully explored[38], we revisit the subcellular localization of SMIM4 and found that SMIM4 is a mitochondrial membrane imbedded protein (Supplementary Fig. 2A–C), with inner membrane localization (Supplementary Fig. 2D). Given the importance of mitochondrial proteins in the control of cellular metabolism[39], we hypothesized that SMIM4 may affect PDAC prognosis via regulating mitochondrial metabolism. Expectedly, Kyoto Encyclopedia of Genes and Genomes (KEGG)-based Gene Set Enrichment Analysis (GSEA) of TCGA-derived transcriptome data from PDAC tissues showed that, patients with higher and lower *SMIM4* expression levels exhibit distinct metabolic performance (Fig. 1H and Supplementary Data 2). Similar results were found in another transcriptome dataset from PDAC tissues (Fig. 1I and Supplementary Data 3). Given the importance of metabolic regulation in PDAC progression[40], these results indicate that the mitochondrial protein SMIM4 may regulate the metabolism of PDAC cells, thereby affecting disease prognosis.

SMIM4 depletion altered metabolic regulation in cultured PDAC cells (Fig. 1J and Supplementary Data 4), but both cell proliferation (Fig. 1K, L) and colony formation (Fig. 1M), which are sensitive to metabolic perturbation, were unaffected by depleting *SMIM4* in two PDAC cell lines. The cell cycle (Supplementary Fig. 3A, B), apoptosis (Supplementary Fig. 3C, D), and cell morphology (Supplementary Fig. 3E, F) were also unaltered in PDAC cells lacking *SMIM4*, which confirms that SMIM4 is dispensable for the growth of PDAC. Consistently, genome-scale CRISPR screening confirmed that *SMIM4* knockout did not affect PDAC cell proliferation (Fig. 1N) (https://depmap.org/portal/). Furthermore, we confirmed that SMIM4 is dispensable for PDAC growth by comparing mice that underwent subcutaneous injection of PANC-1 cells with or without *SMIM4* depletion (Fig. 1O–Q). Therefore, as a favorable prognostic marker for PDAC, SMIM4 may inhibit cancer cell survival or metastasis, rather than suppressing cancer cell proliferation.

SMIM4 depletion does not affect mitochondrial respiration in PDAC cells

The exact SMIM4 function was not known during the course of this study until Peter Rehling et al. claimed that SMIM4 is an assembly factor for respiratory chain complex III assembly[41]. Although interaction between SMIM4 and UQCC1 was detected in MIA PaCa-2 cells as previously described (Fig. 2A)[41], neither *SMIM4* depletion nor knockout in MIA PaCa-2 cells affected complex III and complex III-containing supercomplex assembly (Fig. 2B, C **for *SMIM4* depletion**, Fig. 2D, E **for *SMIM4* knockout**) or mitochondrial respiration and the activity of

https://doi.org/10.1038/s41467-025-64734-y

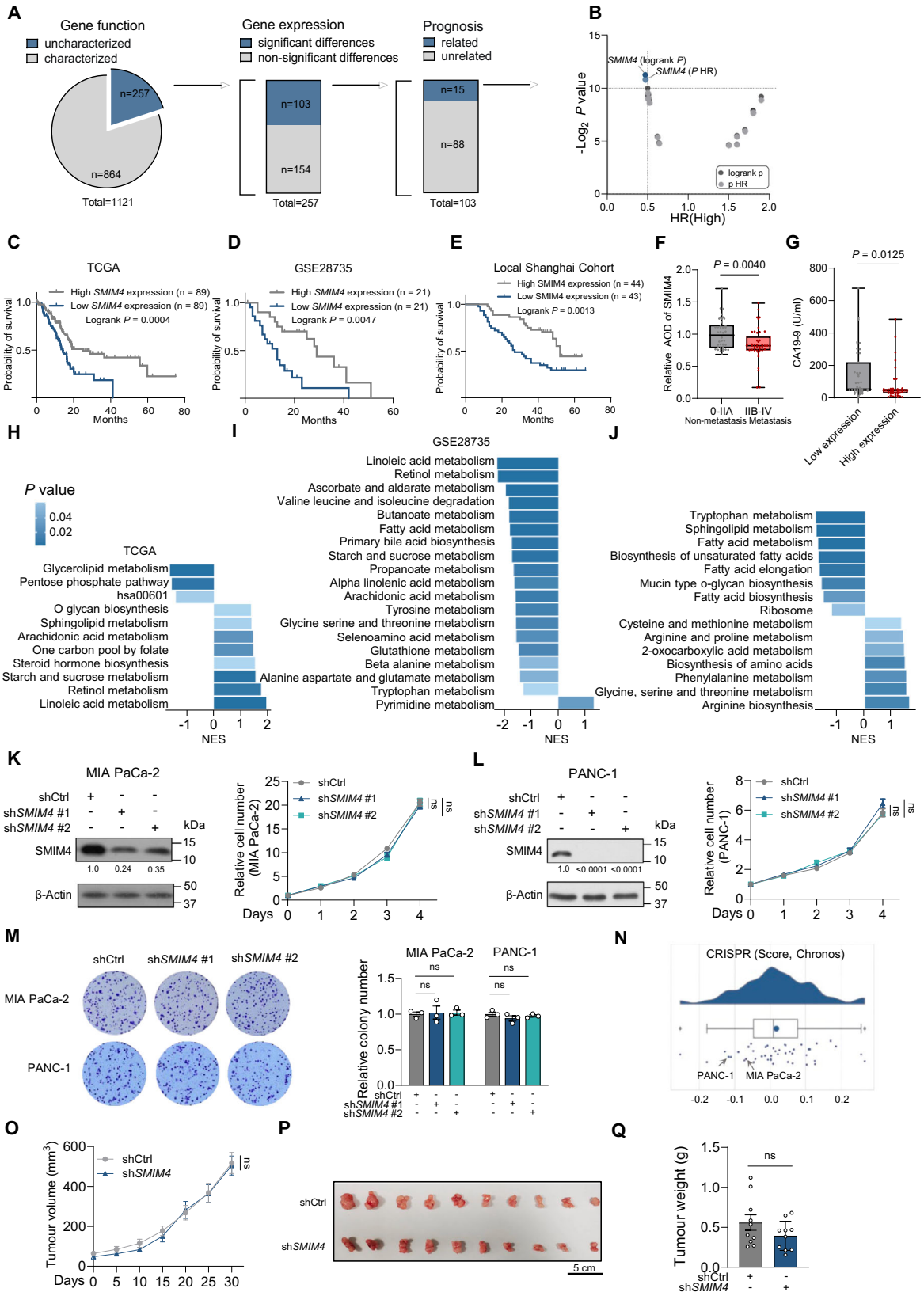

oxidative phosphorylation (OXPHOS) complexes (Fig. 2F, G). The activation of compensatory mitochondrial mechanisms to overcome dysfunctional OXPHOS[42], which may mask *SMIM4* depletion-induced complex III deficiency, was ruled out by measuring the mtDNA copy number (Supplementary Fig. 4A), mtDNA transcription (Supplementary Fig. 4B), and mitochondrial number (Supplementary Fig. 4C, D). Moreover, mitochondrial morphologies as measured by perimeter, area, and cristae width were not affected by *SMIM4* depletion (Fig. 2H–K), and mitochondrial dysfunction-associated transcriptional pathways were not detected by *SMIM4* depletion in MIA PaCa-2 cells when enriched in the gene ontology (GO) and KEGG pathways enrichment analyses were performed (Supplementary Data 4). The

Fig. 1 | SMIM4 is a favorable prognostic biomarker of pancreatic cancer. **A** Criteria and filtering approach for identifying PDAC-associated mitochondrial genes with unknown functions. **B** Log-rank *P* values, HR, and significance for high expression of 15 PDAC-associated mitochondrial genes analyzed using TCGA. **C**–**E** Survival rates analyzed by Log-rank test for patients divided by median SMIM4 expression using TCGA (**C**; high $n = 89$ patients, low $n = 89$ patients), GSE28735 (**D**; high $n = 21$ patients, low $n = 21$ patients), and tissue microarray (**E**; high $n = 44$ patients, low $n = 43$ patients). **F** SMIM4 level in PDAC tumor tissues with and without metastasis (non-metastasis, $n = 42$ patients; metastasis, $n = 45$ patients). **G** CA19-9 level in patients with high and low SMIM4 expression (High $n = 44$ patients; Low $n = 43$ patients). **H**, **I** KEGG pathway enrichment analysis by GSEA was performed on transcriptome data from PDAC tissues, categorized by median expression levels in TCGA (**H**) and GSE28735 dataset (**I**). **J** KEGG pathway enrichment analysis by GSEA of RNA-Seq data from MIA PaCa-2 cells with or without *SMIM4* depletion ($n = 4$ biologically independent samples). **K**, **L** Cell proliferation of MIA PaCa-2 (**K**) and PANC-1 (**L**) cells with or without *SMIM4* depletion in regular medium ($n = 3$ biologically independent samples). **M** Colony formation in crystal violet-stained MIA-PaCa2 and PANC-1 cells with or without *SMIM4* depletion after 10 days of cell culturing ($n = 3$ biologically independent samples). **N** The Chronos dependency score using CRISPR/Cas9 ($n = 47$ pancreatic cancer cell lines). **O**–**Q** Tumor growth curves (**O**) from xenograft mouse models using PANC-1 cells with or without *SMIM4* depletion ($n = 10$ mice). Tumors isolated (**P**) and weighed (**Q**) after 30 days. Scale bar, 5 cm. Data are presented as means ± SEM for bar graphs from at least three independent experiments. Box plots show the 25th–75th percentiles with median; whiskers indicate min-max values. Statistical significance was determined by unpaired two-tailed Student's *t*-test for (**F**, **G**, **K**–**M**, **O**, and **Q**); two-sided permutation test with false discovery rate correction was used for (**H**–**J**). ns not significant. Source data are provided as a Source Data file.

dispensability of SMIM4 in the regulation of mitochondrial respiration was confirmed by detecting the assembly of complex III and the complex III-containing supercomplexes (Supplementary Fig. 4E, F) and mitochondrial respiration (Supplementary Fig. 4G) in PANC-1 cells with *SMIM4* depletion. Collectively, these data strongly support that SMIM4 expression affects PDAC prognosis without changing mitochondrial respiration.

SMIM4 depletion protects PDAC cells from cell death under nutrient-deficient conditions

The prevention of cell death in cancer cells via metabolic reprogramming, particularly in a nutrient-deprived TME, is one of the key contributing factors to the poor prognosis of PDAC[43,44]. Therefore, we cultured PDAC cells in a nutrient-limited medium and found that *SMIM4* depletion in PDAC cells conferred resistance to glucose deprivation-induced cell death (Fig. 3A, B), which was probably due to a decrease in apoptosis (Fig. 3C, D) and lipid peroxidation (Fig. 3E, F) in PDAC cells with *SMIM4* depletion. Moreover, *SMIM4* depletion-induced cell death in MIA PaCa-2 cells cultured with glucose-deficient medium was fully restored by apoptosis inhibitor Z-VAD-FMK (Supplementary Fig. 5A, B), since lipid peroxidation is closely associated and regulate apoptosis[45–47], decreased lipid peroxidation may contribute to lower apoptosis level in *SMIM4*-depleted cells when compared with control cells. Consistently, *SMIM4* depletion protected MIA PaCa-2 cells from cell death (Supplementary Fig. 6A, B) and oxidative stress (Supplementary Fig. 6C, D) when cultured cells with glutamine-deficient medium. Previous studies demonstrated that cancer cells exhibit enhanced glucose or glutamine metabolism to survive in TMEs with limited glutamine or glucose supply[48–50]; thus, we investigated whether SMIM4 promotes glucose and/or glutamine metabolism. To explore this, we cultured *SMIM4*-depleted PDAC cells alongside matched control cells in glucose-deprived medium with titrated glutamine, or glutamine-deprived medium with titrated glucose. Our results indicated that *SMIM4* depletion-induced protection from cell death in PDAC cells is independent of glutamine (Fig. 3G, H) and glucose metabolism (Supplementary Fig. 6E, F).

We found that depletion of *SMIM4* protected PDAC cells from oxidative stress in a glucose-deficient medium (Fig. 3I, J **for MIA PaCa-2 cells**; Supplementary Fig. 6G, H **for PANC-1 cells**). Moreover, this effect is likely attributed to the higher NADPH/$NADP^+$ and GSH/GSSG ratios observed in *SMIM4*-depleted cells compared to those in matched control PDAC cells (Fig. 3K, L **for MIA PaCa-2 cells**, Supplementary Fig. 6I, J **for PANC-1 cells**). Inhibiting oxidative stress in the two PDAC cell lines using NAC and GSH abrogated the difference in the cell survival rates caused by *SMIM4* depletion (Fig. 3M, N **for MIA PaCa-2 cells**, Supplementary Fig. 6K, L **for PANC-1 cells**). However, inhibiting mitochondrial respiration did not contribute to the anti-cell death effect induced by *SMIM4* depletion in MIA PaCa-2 cells cultured in glucose-free medium (Supplementary Fig. 6M), which further excludes the involvement of mitochondrial respiration in PDAC cells with *SMIM4* depletion. To investigate if *SMIM4* depletion sustained GSH availability to exert its anti-cell death effect in PDAC cells cultured in glucose-deficient medium, we depleted the GSH synthesis enzyme GSR in MIA PaCa-2 cells with and without *SMIM4* depletion (Fig. 3O, P). Our findings revealed that the anti-cell death effect of *SMIM4* was completely abolished upon inhibiting GSH generation (Fig. 3Q). In contrast, re-expression of *SMIM4* in *SMIM4*-depleted cells promoted cell death in MIA PaCa-2 cells (Supplementary Fig. 7A, B), as well as apoptosis (Supplementary Fig. 7C) and lipid peroxidation (Supplementary Fig. 7D). Analyses of cellular redox showed that *SMIM4* re-expression enhanced H_2O_2 levels (Supplementary Fig. 7E) and suppressed the NADPH/$NADP^+$ and GSH/GSSG ratios (Supplementary Fig. 7F, G) in *SMIM4*-depleted MIA PaCa-2 cells cultured in glucose-deficient medium. These results indicate that *SMIM4* depletion protects PDAC cells from death, most likely apoptosis, by preserving redox homeostasis in the TME under limited nutrient supplies, such as glucose deficiency.

SMIM4 regulates PDAC cell survival under glucose deprivation via malate-mediated NADPH generation

There are four major metabolic routes for NADPH generation from $NADP^+$ in human cells (Fig. 4A), which maintain the cellular redox balance[21]. While PPP is the primary pathway for NADPH generation, under glucose deprivation condition, *SMIM4*-depleted cells may exhibit a greater tendency towards generating NADPH from at least one of the other three sources compared to that of matched control cells. To test this hypothesis, untargeted metabolic profiling of MIA PaCa-2 cells with or without *SMIM4* depletion under glucose-deficient conditions was performed (Supplementary Data 5). Besides the higher GSH/GSSG ratio, as observed previously (Figs. 3L and 4B), serine and malate levels, which are essential for NADPH generation via the three metabolic pathways (Fig. 4A), were higher in *SMIM4*-depleted MIA PaCa-2 cells compared to those in the matched control cells (Fig. 4B), and exogenous addition of serine (4 mM) or malate (4 mM) abolished such difference (Supplementary Fig. 8A, B). The involvement of serine and citrate in preserving *SMIM4*-depleted cells survival under glucose deprivation was ruled out (Fig. 4C, D), but addition of malate abolished the differences in the cell survival rates (Fig. 4E, F), NADPH/$NADP^+$ (Fig. 4G, H), H_2O_2 levels (Fig. 4I, J), and lipid peroxidation (Fig. 4K, L) between the two PDAC cell groups with and without *SMIM4* depletion in glucose-deficient medium. To investigate the impact of malate supplementation on PDAC cell metabolism with or without *SMIM4* depletion, we conducted untargeted metabolic profiling of MIA PaCa-2 cells with or without *SMIM4* depletion, and with or without malate supplementation under glucose-deficient conditions (Supplementary Data 6). Metabolite set enrichment analysis (MSEA) revealed that malate supplementation abolished changes of "glutathione metabolism" and "alanine, aspartate and glutamate metabolism", two of the seven most affected metabolic pathways due to *SMIM4* depletion (Normalized $P \le 0.05$, metabolites hits/total compounds ≥ 40%) (Fig. 4M), in PDAC cells with or without *SMIM4* depletion when

https://doi.org/10.1038/s41467-025-64734-y

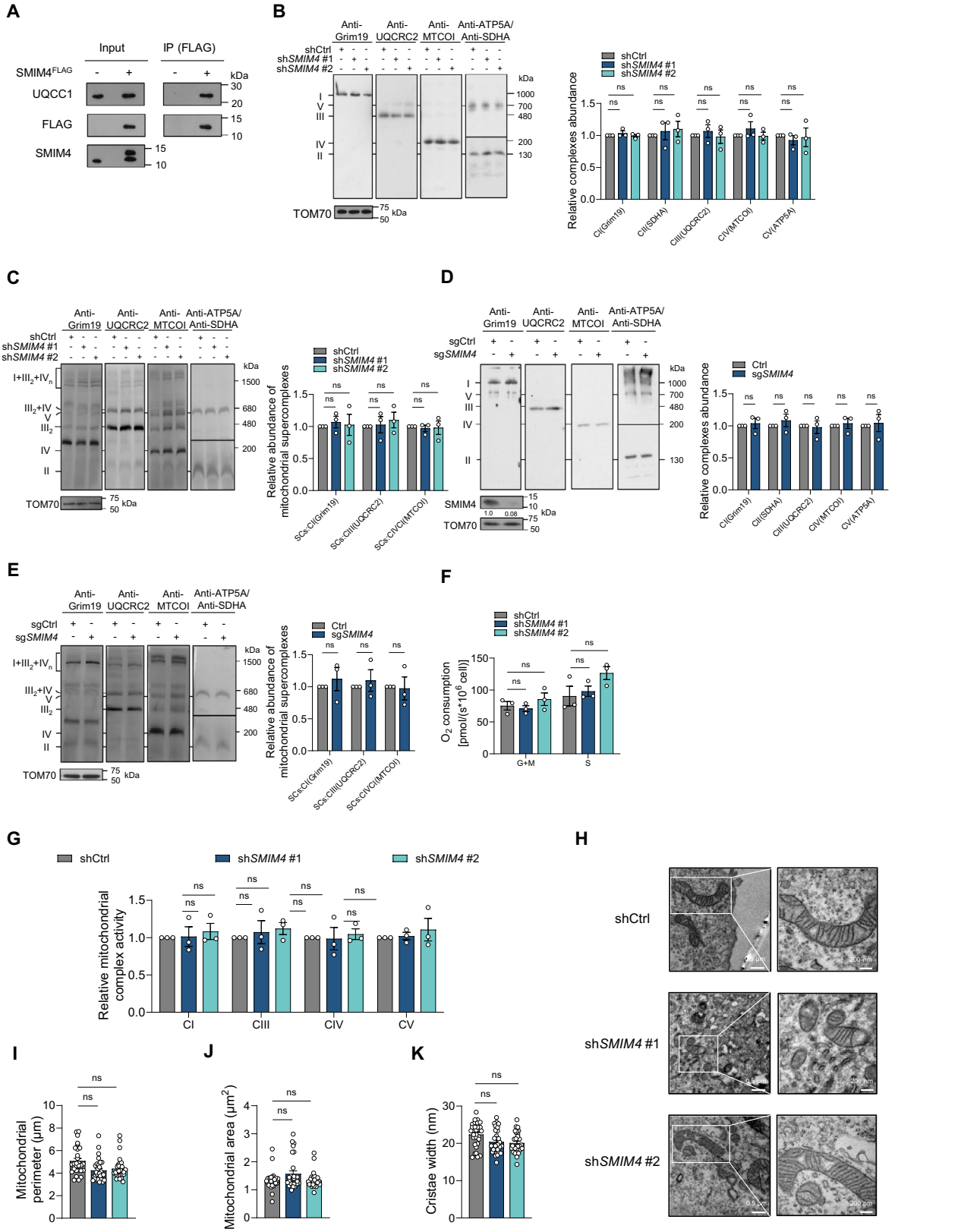

cultured with glucose-deficient conditions. Since malate is closely associated with both 'glutathione metabolism' and "alanine, aspartate and glutamate metabolism"[51–53], and its supplementation also abolished the difference in GSH/GSSG due to *SMIM4* depletion (Fig. 4N), these results, together with Fig. 4G–L, strongly indicate that malate is involved in SMIM4-regulated cellular redox balance by regulating malate associated NADPH metabolism. Furthermore, the levels of precursors of malate, such as aspartate, citrate, and fumarate, did not differ in *SMIM4*-depleted cells cultured in glucose-deprived medium (Fig. 4B and Supplementary Fig. 8C), and all of them have no role in preserving cell survival in *SMIM4*-depleted MIA PaCa-2 cells cultured in glucose-deficient medium (Fig. 4D and Supplementary Fig. 8D, E).

Fig. 2 | Mitochondrial respiration is minimally affected by *SMIM4* depletion in PDAC cells. A Immunoprecipitations of SMIM4^{FLAG}. Eluates were analyzed by SDS-PAGE followed by western blotting with indicated antibodies. Representative images are from three independent biological replicates. **B** Steady-state levels of OXPHOS complexes were analyzed in MIA PaCa-2 cells with or without *SMIM4* depletion ($n = 3$ biologically independent samples). Triton ×-100 solubilized protein was separated by 3.5%–16% BN-PAGE. **C** Respiratory supercomplexes were analyzed in MIA PaCa-2 cells with or without *SMIM4* depletion ($n = 3$ biologically independent samples). Digitonin-solubilized protein was separated by 3%–11% BN-PAGE. **D** Steady-state levels of OXPHOS complexes were analyzed in MIA PaCa-2 cells with or without CRISPR/Cas9-mediated *SMIM4* knockout ($n = 3$ biologically independent samples). Triton ×-100 solubilized protein was separated by 3.5%–16% BN-PAGE. **E** Respiratory supercomplexes were analyzed in MIA PaCa-2 cells with or without CRISPR/Cas9-mediated *SMIM4* knockout ($n = 3$ biologically independent samples). Digitonin-solubilized protein was separated by 3%-11% BN-PAGE. **F** Glutamate and malate (G + M)-dependent, succinate (S)-dependent respiration of MIA PaCa-2 cells with or without *SMIM4* depletion ($n = 3$ biologically independent samples). **G** Relative activities of mitochondrial OXPHOS complexes I–V measured in MIA PaCa-2 cells with or without *SMIM4* depletion and normalized against CII activity ($n = 3$ biologically independent samples). **H** Mitochondrial morphology observed by electron microscopy of MIA PaCa-2 cells with or without *SMIM4* depletion. ×15,000 magnification, scale bar: 0.5 μm; ×50,000 magnification, scale bar: 200 nm. **I–K** Quantitative analysis of mitochondrial perimeter (**I**), the area of individual mitochondria (**J**), and the width of cristae (**K**) in MIA PaCa-2 cells with or without *SMIM4* depletion ($n = 30$ mitochondria per group). Data are presented as means ± SEM for bar graphs from at least three independent experiments. Statistical significance was determined by unpaired two-tailed Student's *t*-test for (**B–G** and **I–K**). ns not significant. Source data are provided as a Source Data file.

Given that exogenous malate rather than aspartate supplementation fully restored both the cellular and cytosolic malate level (Supplementary Fig. 8F, G), indicating that SMIM4 is unlikely involved in malate generation but may mediate its mitochondria to cytosol transportation to support NADPH generation and cellular redox balance, possibly via the conversion of malate to pyruvate (Fig. 4A)[21].

SMIM4 assists the assembly of malate/citrate exchanger complexes that promote malate transportation

To determine the role of SMIM4 in malate metabolism, we performed a co-immunoprecipitation (Co-IP)/mass spectrometry assay in HEK 293 T cells using FLAG-tagged SMIM4. We identified 27 mitochondrial proteins that may interact with SMIM4 (Fig. 5A and Supplementary Data 7), of which only SLC25A1 was involved in malate metabolism, supporting citrate efflux and subsequent malate influx within mitochondria[54]. The interaction between SMIM4 and SLC25A1 was supported by the finding that either *SMIM4* depletion or *SLC25A1* deletion led to the impairment of SLC25A1-containing complexes from 150 to 1500 KDa, while causing an accumulation of a much smaller SLC25A1-containing complex (å 75 and <100 KDa) in *SMIM4* depletion cells (Fig. 5B). Since the total amount of SLC25A1 was not decreased due to *SMIM4* depletion (Fig. 5C), these results together indicate that SMIM4 assists in the assembly of a SLC25A1-containing complex (å 75 and <100 KDa) into a ~150KDa complex. However, whether SMIM4 serve as an assembly factor similar to its role in respiratory chain complex III assembly[41] remains elusive. A recent study identified another mitochondrial small integral membrane protein SMIM26, functions as a connecter between SFXN1 and mitoribosomes[55], also add the possibility that SMIM4 may function as a connecter between SLC25A1 and other proteins yet need to be identified. Both endogenous (Supplementary Fig. 9A, B) and exogenous co-IP/immunoblot (Fig. 5D, E) and the findings of a previous study on SMIM4 (Fig. 5A)[41] further confirm the interaction between SMIM4 and SLC25A1. Bioinformatic analysis using molecular docking and molecular dynamics (MD) simulations[56]. Specifically, possible interactions were observed at SMIM4 (Glu37)-SLC25A1 (Ser193), SMIM4 (Tyr51)-SLC25A1 (Thr122), SMIM4 (Arg55)-SLC25A1 (Met112), and SMIM4 (Gln62)-SLC25A1 (Gln116) (Fig. 5F). Insilco single site mutation assay using MutaBind2[57] indicated that SMIM4 residues Arg55, Tyr51, and Glu37 may participate in SLC25A1 binding (with decreasing likelihood based on ΔΔG bind (kcal/mol) score), while Gln62 has a negligible effect (Fig. 5G), however, Co-IP analyses revealed that only mutations at Tyr51 and Arg55 impaired the interaction between exogenous SMIM4 and SLC25A1 in PDAC cells (Fig. 5H, I), whereas the Glu37 was experimentally ruled out, likely because of the relatively lower ΔΔG associated with this residue and its location in the inner mitochondrial membrane. A GST pull-down assay showed that purified GST-SMIM4 directly interacts with intermembrane space domains of SLC25A1-containing Met112 and Thr 122, confirming a direct interaction between SMIM4 and SLC25A1 (Fig. 5J). Functionally, exogenous re-expression of wild-type SMIM4, SMIM4 (Glu37Lys), and SMIM4 (Gln62Pro), rather than SMIM4 (Tyr51Ser) and SMIM4 (Arg55Trp), abrogated the *SMIM4* knockout-induced anti-cell death and anti-lipid peroxidation in PDAC cells cultured with glucose-deficient medium (Fig. 5K, L). On the contrary, inhibition of SLC25A1 conferred protection against cell death and lipid peroxidation in PDAC cells expressing exogenous wild-type SMIM4, but not in cells expressing the mutant SMIM4 (Y51S and R55W), when cultured under glucose-deficient conditions (Fig. 5M, N). Moreover, BN-PAGE analyses revealed that disrupting SMIM4 and SLC25A1 interaction via SMIM4 (Y51S) and SMIM4 (R55W) impaired the formation of SLC25A1-containing complexes from 150 to 1500 KDa (Fig. 5O) and led to the accumulation of a small SLC25A1-containing complex (å 75 and <100 KDa) as we observed in Fig. 5B. Our results therefore revealed that Tyr51 and Arg55 in SMIM4 are required not only for the interactions between SMIM4 and SLC25A1 but also for the functionality of SMIM4 and SLC25A1 in PDAC cells.

Given that inhibitor (CTPI-2)-induced *SLC25A1* and *SMIM4* depletion both increased cellular and cytosolic malate levels, *SMIM4* depletion failed to elevate these levels in SLC25A1 inhibited cells compared to control cells with SLC25A1 inhibition (Fig. 5P, Q), which suggests that SMIM4 may directly interact with SLC25A1 to mediate citrate and malate transportation. To determine whether SMIM4 regulates citrate/malate transportation, we monitored citrate metabolism via both [U-^{13}C] glucose and [U-^{13}C] glutamine labelling as previously described[58]. In the [U-^{13}C] glutamine labelling assay, an m + 4-labeled citrate from [U-^{13}C] glutamine generated m + 2-labeled malate in the TCA cycle, whereas efflux of m + 4-labeled citrate into the cytosol led to the generation of m + 4-labeled malate (Fig. 5R). The higher ratio of malate m + 2/citrate m + 4 in *SMIM4*-depleted PDAC cells indicated a decrease in the output of citrate in *SMIM4*-depleted cells compared to that in the matched control cells (Fig. 5S), whereas *SMIM4* depletion did not affect citrate output in PDAC cells with SLC25A1 blockage (Fig. 5T). Indicating the requirement of SLC25A1 on SMIM4 mediated citrate output from mitochondria. In the [U-^{13}C] glucose labelling assay, m + 2-labeled citrate from [U-^{13}C] glucose led to the generation of m + 2- and m + 0-labeled malate in the TCA cycle and cytosol (Fig. 5U), respectively[58], the higher ratio of malate m + 2/citrate+2 in *SMIM4*-depleted cells compared with control cells again indicated a lower output of citrate from the mitochondria into the cytosol due to *SMIM4* depletion (Fig. 5V). Although either *SMIM4* deletion or SLC25A1 inhibition impaired malate uptake into isolated mitochondria, *SMIM4* deletion did not further reduce malate uptake in cells with genetic depletion or pharmacological inhibition of SLC25A1 (Fig. 5W, X). All these results together strongly suggest that SMIM4 facilitates malate/citrate transportation by interacting with SLC25A1.

SMIM4 depletion protects PDAC cells from death under glucose deprivation by blocking malate/citrate transporter

To explore whether blockage of malate/citrate transportation protects cells from death under glucose deprivation, we cultured PDAC cells

https://doi.org/10.1038/s41467-025-64734-y

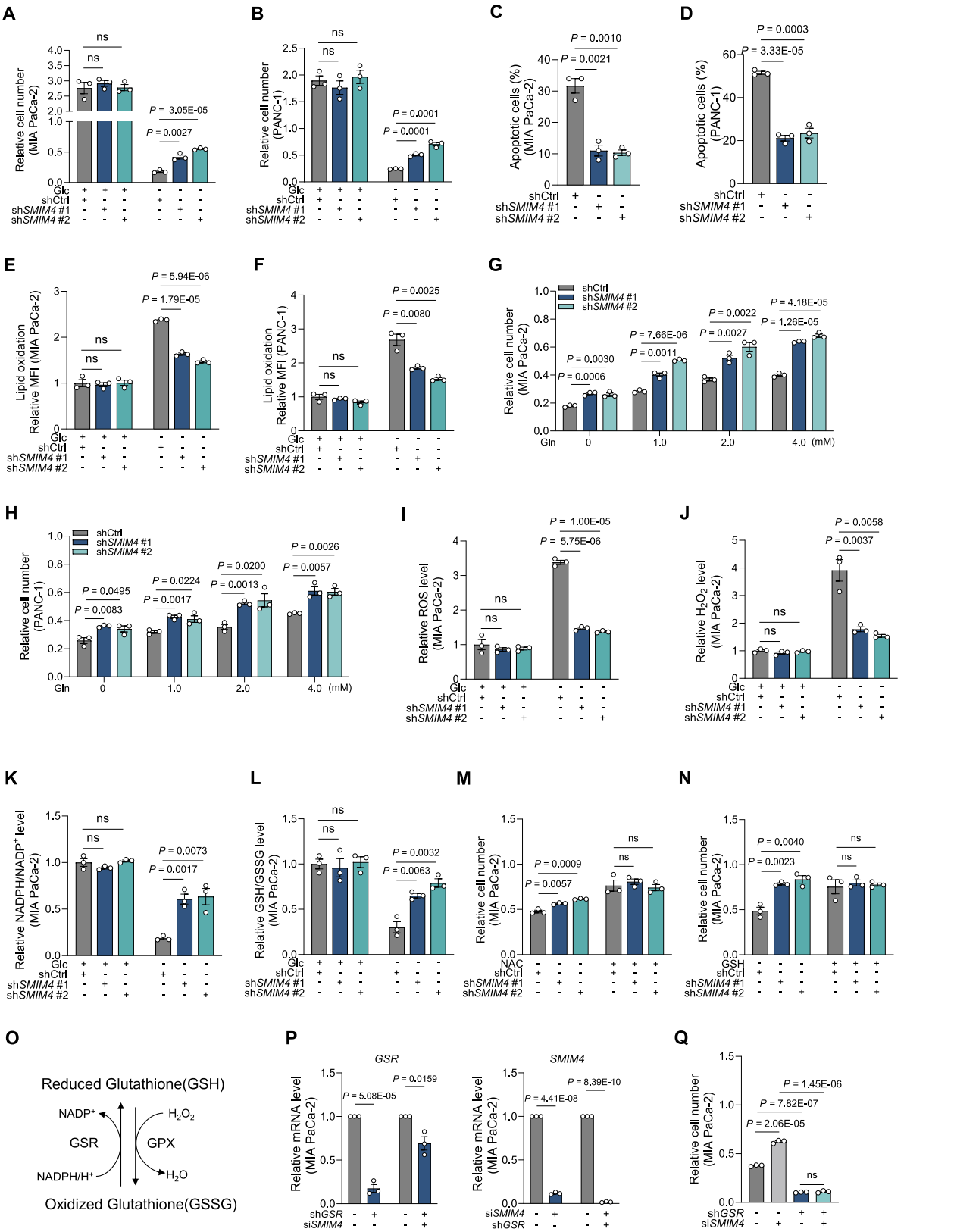

with or without CTPI-2 and found that CTPI-2 inhibition protected PDAC cells from death (Fig. 6A, B). Moreover, CTPI-2 treatment led to increased cellular and cytosolic malate (Fig. 5P, Q), and exogenous administration of malate increased cell survival compared with that of CTPI-2 treated cells cultured under glucose deficiency (Fig. 6A, B). Measurement of cellular redox showed that CTPI-2 treatment decreased H_2O_2 levels and increased NADPH/NADP$^+$ ratio to a similar extent in the two PDAC cell lines cultured in glucose-deficient medium (Fig. 6C, D **for MIA PaCa-2 cells;** Fig. 6E, F **for PANC-1 cells**). These results indicate that, by preserving cellular redox homeostasis, accumulated cytosolic malate caused by blockage of the malate/citrate transporter increases cell survival under glucose deprivation.

Fig. 3 | *SMIM4* depletion protects PDAC cells from glucose deprivation induced cell death. A–F Cell number (**A**, **B**), apoptosis (**C**, **D**), and lipid peroxidation (**E**, **F**) level in MIA PaCa-2 and PANC-1 cells with or without *SMIM4* depletion in the presence and absence of glucose for 24 h ($n = 3$ biologically independent samples). **G**, **H** Cell number of MIA PaCa-2 (**G**) and PANC-1 (**H**) cells with or without *SMIM4* depletion under culture conditions of 0, 1, 2, and 4 mM glutamine in the absence of glucose for 24 h ($n = 3$ biologically independent samples). **I–L** ROS (**I**), H_2O_2 (**J**), NADPH/NADP$^+$ (**K**), GSH/GSSG (**L**) level of MIA PaCa-2 cells with or without *SMIM4* depletion in the presence and absence of glucose for 24 h ($n = 3$ biologically independent samples). **M, N** Cell number of MIA PaCa-2 cells with or without *SMIM4* depletion in the absence of glucose or in the absence of glucose supplemented with 40 μM NAC (**M**), 40 μM GSH (**N**) for 24 h. MIA PaCa-2 cells were pretreated with NAC or GSH for 24 h before culture in glucose-deprived medium ($n = 3$ biologically independent samples). **O** Schematic representation of glutathione reductase (GSR)-mediated glutathione (GSH) metabolism. **P** mRNA level of *GSR* and *SMIM4* in MIA PaCa-2 cells with *GSR* and *SMIM4* depletion, respectively ($n = 3$ biologically independent samples). **Q** Cell number of MIA PaCa-2 cells with or without *GSR* depletion, transfected with ctrl siRNA or *SMIM4* siRNA in the absence of glucose for 24 h ($n = 3$ biologically independent samples). Data are presented as means ± SEM for bar graphs from at least three independent experiments. Statistical significance was determined by unpaired two-tailed Student's *t*-test for (**A**–**N**, **P**, and **Q**). ns not significant. Source data are provided as a Source Data file.

To determine whether *SMIM4* depletion relies on the inhibition of the malate/citrate transporter to prevent cell death in PDAC cells cultured without glucose, malate/citrate transportation was inhibited by CTPI-2 or depletion of *SLC25A1* in cells with or without *SMIM4* depletion. We found that *SMIM4* depletion increased PDAC cell survival in cells without rather than with inhibition of malate/citrate transportation, when cultured cells with glucose-deprived condition (Fig. 6G, H and Supplementary Fig. 10A **for MIA PaCa-2 cells;** Fig. 6I, J and Supplementary Fig. 10B **for PANC-1 cells**). Inhibition of the malate/citrate transporter has been shown to alter the cellular NADH/NAD$^+$ ratio[58,59], and changes in the ratio contributes to ROS, hydrogen peroxide, NADP, and NADPH generation[60,61]. Although decreased NADH/NAD$^+$ ratio in whole cells (Supplementary Fig. 11A, B) and mitochondria (Supplementary Fig. 11C, D), and increased NADH/NAD$^+$ ratio (Supplementary Fig. 11E, F) in cytosol were detected due to either *SMIM4* depletion or SLC25A1 inhibition in PDAC cells with or without glucose deprivation, eliminating differences in the NADH/NAD$^+$ ratio by promoting NAD+ generation with NAM or NADH oxidation with AKB (Supplementary Fig. 11G, H), did not abolish the protective role of *SMIM4* depletion in PDAC cells survival under glucose deprivation condition (Supplementary Fig. 11I, J). *SMIM4* depletion may also promote pyruvate generation from malate, suppress fatty acid synthesis from citrate[62,63], and enhance malate transport via the malate-aspartate shuttle[64] (Supplementary Fig. 12A). However, inhibiting pyruvate oxidation with UK5099 (Supplementary Fig. 12B), fatty acid synthesis with TOFA (Supplementary Fig. 12C), and the malate/aspartate shuttle with PLP or NPM (Supplementary Fig. 12D, E) failed to eliminate the differences in cell survival between MIA PaCa-2 cells with or without *SMIM4* depletion under glucose-deficient conditions.

Notably, depletion of *ME1*, but not *ME2* (Supplementary Fig. 12F, G **for MIA PaCa-2 cells;** Supplementary Fig. 12H, I **for PANC-1 cells**), (two isoenzymes required for converting malate to pyruvate) fully abolished the protective effect of *SMIM4* depletion on cell survival under glucose deprivation (Fig. 6K, L **for MIA PaCa-2 cells**, Fig. 6M, N **for PANC-1 cells**). These results further support that the anti-cell death effect of *SMIM4* depletion in glucose-deficient medium is mediated by the cytosolic conversion of malate to pyruvate. Meanwhile, in PDAC cells cultured in glucose-deficient medium, *SMIM4* and *SLC25A1* depletion led to a similar decrease in H_2O_2 levels and increase in the NADPH/NADP$^+$ ratio, but co-depletion of *SMIM4* and *SLC25A1* did not induce a synergistic effect on H_2O_2 levels and the NADPH/NADP$^+$ ratio (Fig. 6O, P **for MIA PaCa-2 cells;** Fig. 6Q, R **for PANC-1 cells**). Together, these data suggest that *SMIM4* depletion protects cells from death under glucose deprivation via redistribution of the anti-oxidative metabolite malate in the cytosol by blocking the malate/citrate transporter.

SMIM4 expression predicts the therapeutic efficacy of ferroptosis inducers in PDAC

Given that balanced NADPH/NADP$^+$ and GSH/GSSG ratios are required to protect cells from lipid peroxidation[65,66], which is a hallmark of ferroptosis, we hypothesized that *SMIM4* depletion may protect PDAC cells from ferroptosis by enhancing their anti-oxidative capacity. To test this, MIA PaCa-2 cells with or without *SMIM4* depletion were treated with Ras-selective lethal small molecule 3 (RSL3, a ferroptosis activator). MIA PaCa-2 cells with *SMIM4* depletion showed greater resistance to RSL3-induced cell death than control cells when cultured in glucose-deficient medium, and this effect was abolished by alleviating the oxidative stress with NAC (Fig. 7A). Accordingly, MIA PaCa-2 control cells treated with RSL3 exhibited increased cellular ROS and lipid peroxidation, whereas RSL3 treatment had limited effect on cells with *SMIM4* depletion (Supplementary Fig. 13A and Fig. 7B), consistent results were also observed in PANC-1 cells (Supplementary Fig. 13B and Fig. 7C, D). Treatment with an inducer of H_2O_2 showed that depleting *SMIM4* has potential to protect PDAC cells from cell death (Supplementary Fig. 13C, D), inhibit cellular ROS generation (Supplementary Fig. 13E, F) and lipid peroxidation (Supplementary Fig. 13G, H). Moreover, PDAC cells with relatively higher SMIM4 levels (Fig. 7E) were more sensitive to RSL3- and H_2O_2-induced cell death (Fig. 7F, G).

By looking at *Pdx1-Cre/Kras$^{G12D/+}$/Trp53R$^{172H/+}$* (KPC) mice derived KPC cells, *SMIM4* depletion led to a reduction in ~480 KDa and ~680 KDa SLC25A1-containing complexes (Supplementary Fig. 14A, B), consistent with findings in human PDAC cells (Fig. 5B and O). *SMIM4* depletion also protected cells from death (Supplementary Fig. 14C), increased the cellular NADPH/NADP$^+$ ratio and reduced lipid peroxidation (Supplementary Fig. 14D, E) when cultured in glucose-deficient rather than high-glucose medium. As consistent with human PDAC cells, although both *SMIM4* depletion and SLC25A1 inhibition protected KPC cells from death (Supplementary Fig. 14F), increased the NADPH/NADP$^+$ ratio (Supplementary Fig. 14G), and reduced lipid peroxidation (Supplementary Fig. 14H). However, *SMIM4* depletion failed to confer these effects in cells with SLC25A1 inhibition when cultured in glucose-deficient medium. Consistently, *SMIM4* depletion protected KPC cells from IKE (imidazole ketone erastin, ferroptosis inducer) induced cell death, which was abolished by alleviating the oxidative stress with NAC (Supplementary Fig. 14I).

In vivo studies further confirmed that human PDAC tumor with higher SMIM4 expression in nude mice are more sensitive to ferroptosis-induced inhibition of tumor growth (Fig. 7H–J). This was supported by the finding that IKE supplementation significantly increased level of MDA and 4-HNE (Fig. 7K and L), two lipid peroxidation biomarkers in vivo, in SMIM4-high cells compared to that in SMIM4-low cells. By using a KPC mice derived orthotopic allograft (GDA) model with a more aggressive phenotype than xenograft model[67], we found that mouse PDAC tumor with higher SMIM4 expression were more sensitive to ferroptosis-induced tumor growth inhibition (Supplementary Fig. 14J, K). Moreover, IKE treatment resulted in improved survival outcomes in mice with tumors expressing higher SMIM4 levels compared to those with lower SMIM4 expression (Supplementary Fig. 14L). This effect was likely due to IKE-induced lipid peroxidation, which was more pronounced in tumors with higher SMIM4 expression (Supplementary Fig. 14M, N).

Consistently, tumors with SLC25A1 inhibition were also sensitive to ferroptosis-induced tumor growth inhibition (Supplementary Fig. 15A–C) and exhibited increased lipid peroxidation levels (Supplementary Fig. 15D, E). In contrast, SMIM4 depletion in tumors with

https://doi.org/10.1038/s41467-025-64734-y

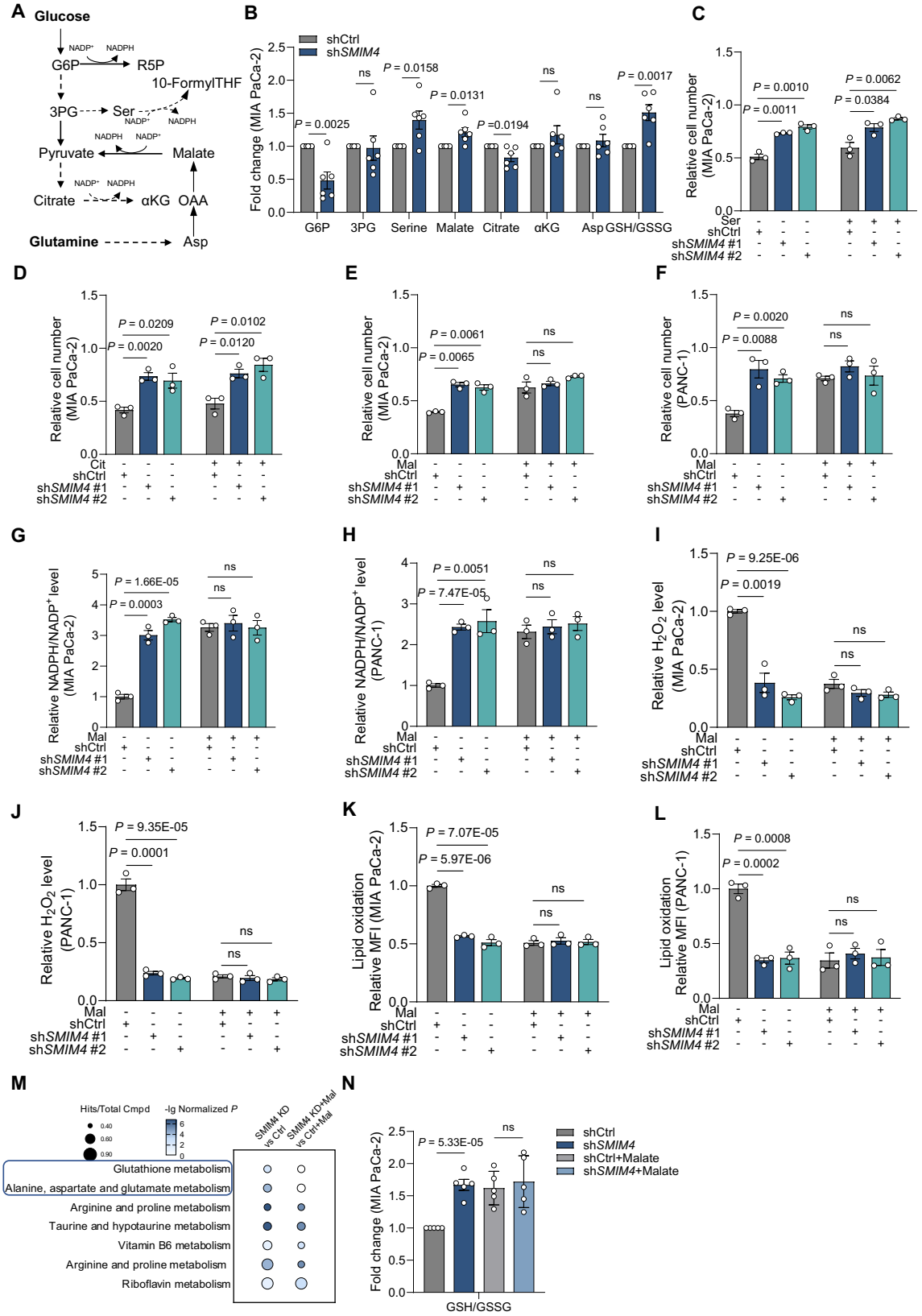

SLC25A1 inhibition did not show sensitivity to ferroptosis-induced inhibition of tumor growth compared to tumors with SLC25A1 inhibition alone (Supplementary Fig. 15A–E), indicating that SMIM4 regulates the sensitivity to ferroptosis-induced inhibition of tumor growth via SCL25A1. Our in vivo studies using human and mouse PDAC cells support the notion that SMIM4 expression is negatively associated with the therapeutic efficacy of IKE treatment. Notably, higher SMIM4 levels in clinical resected human PDAC tumors are significantly associated with increased 4-HNE, a lipid peroxidation maker (Fig. 7M, N). All these results together indicate that SMIM4 expression may be an effective biomarker of therapeutic efficacy for ferroptosis inducer treatment of PDAC.

Fig. 4 | *SMIM4* depletion promotes malate-mediated NADPH production and supports PDAC cells survival under glucose deprivation. A Schematic representation of the primary metabolic pathways generating NADPH from glucose and glutamine. **B** NADPH metabolism-related metabolite levels of MIA PaCa-2 cells with or without *SMIM4* depletion in the absence of glucose for 24 h ($n = 6$ biologically independent samples). **C**–**E** Cell number of MIA PaCa-2 cells with or without *SMIM4* depletion in the absence of glucose or in the absence of glucose supplemented with 4 mM serine (**C**), 2.5 mM citrate (**D**), 4 mM malate (**E**) for 24 h ($n = 3$ biologically independent samples). **F** Cell number of PANC-1 cells with or without *SMIM4* depletion in the absence of glucose or in the absence of glucose supplemented with 4 mM malate for 24 h ($n = 3$ biologically independent samples). **G**–**L** NADPH/$NADP^+$ (**G**, **H**), H_2O_2 (**I**, **J**), and lipid peroxidation (**K**, **L**) level of MIA PaCa-2 and PANC-1 cells with or without *SMIM4* depletion in the absence of glucose supplemented with or without 4 mM malate for 24 h ($n = 3$ biologically independent samples). **M** Metabolite Set Enrichment Analysis (MSEA) of metabolomic data from MIA PaCa-2 cells with or without *SMIM4* depletion in the absence of glucose or in the absence of glucose supplemented with 4 mM malate for 24 h. **N** GSH/GSSG level of MIA PaCa-2 cells with or without *SMIM4* depletion in the absence of glucose or in the absence of glucose supplemented with 4 mM malate for 24 h ($n = 5$ biologically independent samples). Data are presented as means ± SEM for bar graphs from at least three independent experiments. Statistical significance was determined by unpaired two-tailed Student's *t*-test for (**B**–**L** and **N**). Two-sided permutation test with false discovery rate correction was used for (**M**). ns not significant. Source data are provided as a Source Data file.

Discussion

Cancer cells rely on NADPH for the biosynthesis of macromolecular and maintenance of antioxidant capacity[68]. Most NADPH is generated from $NADP^+$ via four metabolic routes: PPP, one carbon metabolism, malate to pyruvate conversion, and isocitrate to αKG conversion[21,68]. Glucose- and glutamine-driven NADPH generation via PPP and malate to pyruvate conversion, respectively, were previously considered necessary for PDAC cell survival[23,69]. However, the nutrient-deprived TME of PDAC tumors forces cancer cells to reprogram their metabolism to maximize NADPH generation for survival[70]. Increased activity or expression of key metabolic enzymes, such as MDH1 via the downregulation of arginine methylation in aspartate to pyruvate conversion[71] or IDH1 overexpression in isocitrate to αKG conversion[72], occur in PDAC cells to support NADPH generation. Particularly, PDAC cells requires GOT1 mediated glutamine metabolism for NADPH generation and cell survival, whereas glutamine was found as a death inducer in mouse embryonic fibroblasts (MEF) cells[23,73], which highlight the cell type specific role of nutrient metabolism. In this study, we identified enzyme-independent regulation of NADPH production in PDAC cells, involving the redistribution of the malate flux between the cytosol and mitochondria. We found that the mitochondrial inner membrane protein SMIM4 interacts SLC25A1, thereby aiding the exchange of mitochondrial citrate for cytosolic malate. In PDAC cells with low SMIM4 levels, transportation of malate into the mitochondria was suppressed, and NADPH levels were higher due to increased malate to pyruvate conversion in the cytosol, protecting PDAC cells from nutrient stress-induced cell death. Furthermore, we found that patients with PDAC and low SMIM4 expression exhibited poor prognosis, which may be partially due to reduced lipid peroxidation. Since PDAC tumors with low SMIM4 expression were resistant to ferroptosis, our results further highlight that SMIM4 expression is an effective biomarker of therapeutic efficacy for the treatment of PDAC with ferroptosis inducers (Fig. 8).

SMIM4 is a member of a small integral membrane proteins (SMIMs), which are largely uncharacterized. SMIM4 was identified as a mitochondria-localized protein based on a large-scale proteomics study[38]. The functional relevance of SMIM4 was initially determined through mitoribosome-interactome analysis of mice hearts and was further characterized as an assembly factor for respiratory chain complex III assembly with C12ORF73[41,74]. Although we confirmed that SMIM4 interacts with C12ORF73, another complex III assembly factor as reported previously[41,75], and some complex III subunits, both shRNA- and CRISPR/Cas9-mediated *SMIM4* depletion in PDAC cells did not impact complex III assembly nor mitochondrial respiration and morphology. Notably, interactions between SMIM4 with the mitoribosome was tissue specific[74], and many other non-OXPHOS mitochondrial proteins were also found to interact with SMIM4, with high similarity between our findings and others[41]. Moreover, the loss of complex III assembly factors generally leads to the disruption of matured complex III[76,77], but *SMIM4* depletion only led to a minor decrease in complex III abundance[41]. Similar results were also detected in *C12ORF73*-depleted cells, in which *C12ORF73* depletion minimally affected complex III assembly, and C12ORF73 was found to have an additional role in regulating pyruvate metabolism[78]. Assembly factors of OXPHOS complexes are multi-functional; for example, ACAD9 is not only a complex I assembly factor but is also required for fatty acid oxidation[79]; therefore, it is highly likely that SMIM4 may either perform a malate/citrate transportation role or serve as a complex III assembly factor in a tissue-specific manner.

A recent study claimed that SLC25A1 functions as a monomer when the detergent LMNG is used to solubilize membrane proteins[80]; however, SLC25A1 was detected in a dimerized form when LMNG is replaced with digitonin[81]. When using digitonin, our findings confirmed that SLC25A1 assembled into large complexes, and a considerable proportion of SLC25A1 proteins were detected with weights ranging from 150 KDa to ~1.5 MDa. While SLC25A1 executes malate/citrate transportation in a monomer state, it is possible that other proteins, such as AFG3L2, interact with mitochondrial metabolic transporters for protein homeostasis[82,83]. Given that *SMIM4* depletion increased SLC25A1 expression but decreased malate transportation efficiency and the amount of SLC25A1-containing complexes, it is likely that an effective metabolic channel exists for citrate/malate metabolism among the complexes containing SLC25A1 and the other uncharacterized enzymes[68,84]. Therefore, SMIM4 may serve as an assembly factor to facilitate the formation of such metabolic channels. Overall, further studies are warranted to fully understand the function of SMIM4 in SLC25A1 related citrate/malate transportation.

Blockage of malate and citrate exchange with CTPI-2 led to decreased NADPH expression[85], likely due to the conversion of cytosolic citrate into pyruvate prior to NADPH generation via a metabolic cascade reaction. Nevertheless, citrate catabolism in the cytosol is needed for fatty acid and cholesterol synthesis, which exhaust NADPH generated from citrate to pyruvate conversion[21,68], particularly in cells in glucose-deficient conditions with reduced PPP-mediated NADPH generation[86]. In this study, we found that inhibition of malate and citrate exchange by *SMIM4* depletion or SLC25A1 inhibition altered malate compartmentalization and induced malate to pyruvate metabolism in the cytosol rather than in the mitochondria. Notably, as previously reported[87], we were surprised that SLC25A1 inhibition led to an increase in cytosolic and cellular malate level. On one hand, the decreased NADH/NAD^+ ratio in mitochondria (Supplementary Fig. 11C, D), and the increased NADH/NAD^+ ratio in the cytosol (Supplementary Fig. 11E, F) due to either *SMIM4* or *SLC25A1* depletion may promote malate generation in cytosol and its conversion to oxaloacetate in mitochondria via malate-aspartate shuttle[52]; on the other hand, citrate accumulation in mitochondria may enhance oxaloacetate and aspartate production through pyruvate carboxylation[88], thereby increasing oxaloacetate flux into the malate-aspartate shuttle and supporting malate generation in the cytosol. Given this, the malate-aspartate shuttle and malate/citrate antiporter may cooperate with each other for malate transportation, the overload of malate-alpha ketoglutarate antiporter may require malate/citrate antiporter for better malate shuttling; lastly, the culture medium containing calf serum includes malate, which increases further during the culture

https://doi.org/10.1038/s41467-025-64734-y

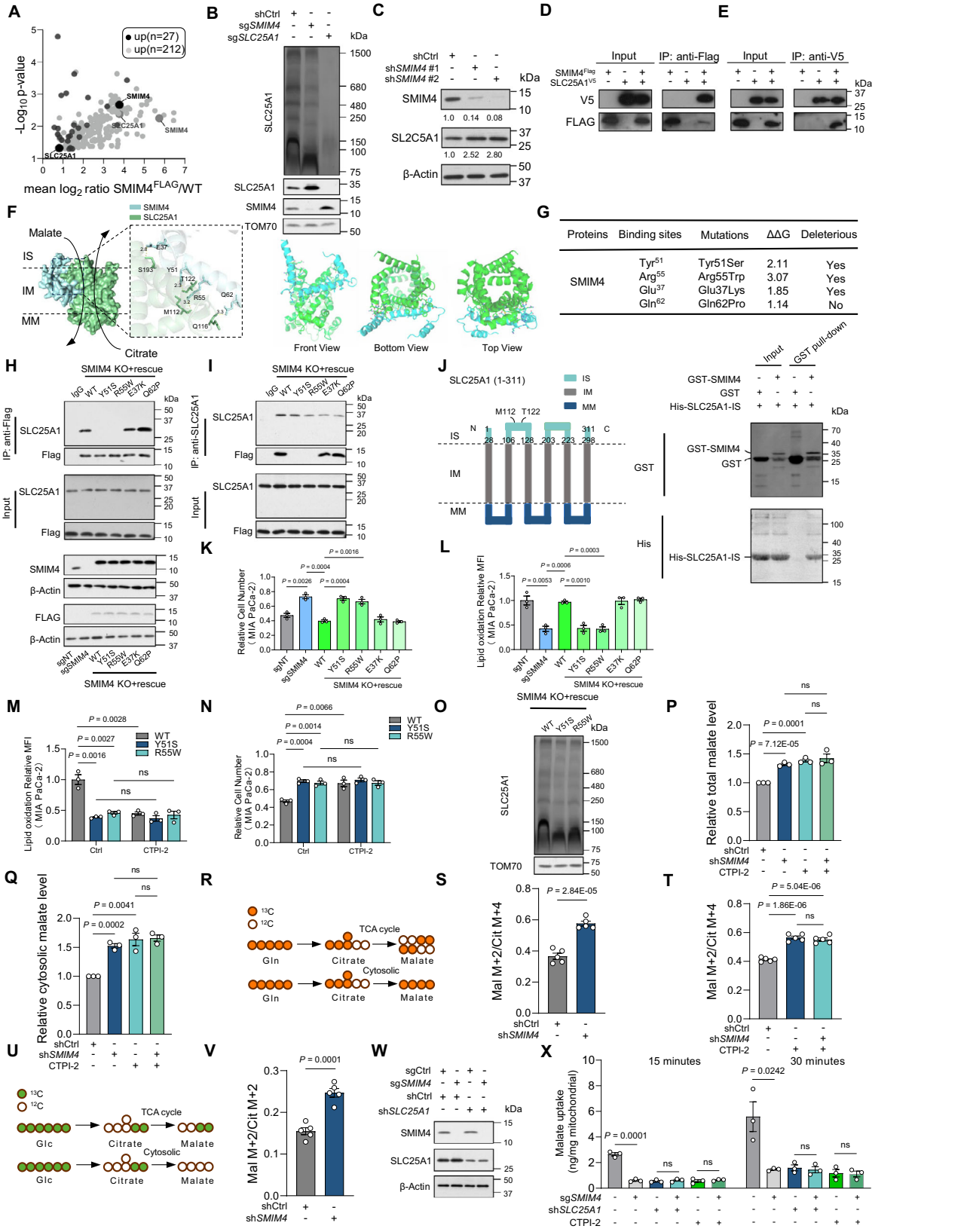

period due to the secretion of malate from the PDAC cell. Since malate can be taken up from the extracellular environment with high affinity[89], blocking the malate/citrate antiporter may restrict the mitochondrial entry of exogenous malate, further contributing to its accumulation in PDAC cells. However, further studies focusing on malate metabolism are required to fully address this concern.

While mitochondrial malate to pyruvate conversion via malic enzyme 2 (ME2) prefers NAD^+ rather than $NADP^+$[90], redistributing malate in the cytosol may promote NADPH generation by ME1, which has robust NADPH generation activity and protect cells from oxidative stress, such as increased ROS an lipid peroxidation[91]. All these data together support the notion that *SMIM4* is a prognostic marker for

Fig. 5 | SMIM4 is required for SLC25A1-mediated mitochondrial malate/citrate transportation. A Mitochondrial extracts from WT and SMIM4-FLAG HEK-293T cells analyzed by native IP and quantitative LC-MS/MS. Black: published data[41], Gray: our experimental results ($n = 3$ biologically independent samples). **B** 3%–12.5% BN-PAGE/immunoblot analysis of SLC25A1 in WT, *SMIM4*-depleted, and *SLC25A1*-knockout MIA PaCa-2 cells. **C** WB of SMIM4 and SLC25A1 in MIA PaCa-2 cells with or without *SMIM4* depletion. **D**, **E** FLAG or V5-immunoisolation of HEK-293T cells expressing SMIM4 ^{FLAG}, SLC25A1 ^{V5}, or both. **F** Molecular docking of SMIM4 with SLC25A1. **G**. Predicted ΔΔG_bind changes for interface mutations. **H**, **I** FLAG- and SLC25A1-immunoisolation in *SMIM4* knockout MIA PaCa-2 cells rescued with WT or mutant SMIM4 variants. **J** Schematic of SLC25A1 sublocalization and sequence features and in vitro Co-IP of GST-SMIM4 with His-SLC25A1-IS. **K**–**N** Cell number (**K**, **N**) and lipid peroxidation (**L**, **M**) in WT, sg*SMIM4*, and sg*SMIM4* cells rescued with SMIM4 variants under 24 h glucose deprivation ± 10 μM CTPI-2 ($n = 3$ biologically independent samples). **O** 3%–12.5% BN-PAGE/immunoblot analysis of SLC25A1-containing complexes in sg*SMIM4* cells rescued with various SMIM4 variants in MIA PaCa-2 cells. **P**, **Q** Cellular (**P**) and cytosolic (**Q**) malate levels in MIA PaCa-2 cells with or without *SMIM4* depletion, under 24 h glucose deprivation ± 10 μM CTPI-2 ($n = 3$ biologically independent samples). **R**–**V** Schematics illustrate potential fates of citrate derived from glutamine (**R**) or glucose (**U**). Fractional enrichment ratios (**S**, **T**, **V**) in MIA PaCa-2 cells with or without *SMIM4* depletion and treatments as indicated ($n = 5$ biologically independent samples). **W** WB of SMIM4 and SLC25A1 in MIA PaCa-2 cells with or without *SMIM4*-KO and *SLC25A1* depletion. **X** Malate uptake in isolated mitochondria from MIA PaCa-2 cells with or without *SMIM4*-KO or *SLC25A1* depletion or CTPI-2 treatment ($n = 3$ biologically independent samples). Data are presented as means ± SEM for bar graphs from at least three independent experiments. Representative images for (**B**–**E**, **H**–**J**, **O**, and **W**) are from three independent biological replicates. Statistical significance was determined by unpaired two-tailed Student's *t*-test for (**A**, **K**–**N**, **P**, **Q**, **S**, **T**, **V**, and **X**). ns not significant. Source data are provided as a Source Data file.

PDAC, and high SMIM4 expression correlates with better prognosis and sensitivity to ferroptosis inducers. Notably, although we focused on the regulatory role of SMIM4 in lipid peroxidation under nutrient-poor condition, we also found that glucose deprivation led to increased lipid peroxidation. However, other studies have shown that glucose deprivation protects cells from lipid peroxidation through AMPK or PDK4 activation in MEFs and PDAC cells[92,93]. Furthermore, a previous study showed that glucose slightly protects cells from RSL3- or FIN56-induced cell death, but not erastin-induced death, in some PDAC cells[92], highlighting the cell-type-specific role of glucose availability in response to ferroptosis induction. Moreover, differences in cell culture conditions between studies, such as whether serum is dialyzed to exclude glucose-related carbon sources, should also be noted. It is likely that AMPK and PDK4 activation reduce lipid peroration, but raise the possibility that low-to-negligible level of glucose-induced oxidative stress may also contribute to increased lipid peroxidation, the balance of which may altered based on how glucose was depleted and the cell types we used; however, further studies are required to fully address this issue. The regulatory mechanism of SMIM4 and whether dual targeting of SMIM4 expression and ferroptosis may facilitate the treatment of PDAC also need further validation.

In summary, our study found that SMIM4 interacts with SLC25A1 and mediates malate/citrate transportation. Low SMIM4 expression impairs the assembly of SLC25A1 complexes, reshapes the -compartmentalization malate distribution, and promotes malate-associated NADPH generation in the cytosol of PDAC cells, protecting PDAC cells from death under nutrient-deficiency induced oxidative stress.

Methods

Ethical considerations

This study was conducted in full compliance with all relevant ethical regulations. All animal experiments were performed in accordance with protocols approved by the Laboratory Animal Ethics Committee of Wenzhou Medical University (approval No. wydw2022-0589). The Wenzhou patient cohort ($n = 28$ patients) was approved under ethics protocol No. 2017-159 by the Ethics Committee of The First Affiliated Hospital of Wenzhou Medical University. The Shanghai patient cohort ($n = 87$ patients) was approved by the Institutional Ethics Review Board of Shanghai Outdo Biotech (Shanghai, China; approval No. SHYJS-BC-2310001).

Patient samples

Patients included both male and female individuals. All patients, irrespective of age, with a pathologically confirmed diagnosis of PDAC at one of the participating centers and from whom sufficient tumor tissue was available for analysis were eligible. This included patients at primary diagnosis as well as those with disease progression or relapse. The study included patients from two centers: 28 patients from The First Affiliated Hospital of Wenzhou Medical University (ethics protocol No. 2017-159) and 87 patients from Shanghai Outdo Biotech (Shanghai, China; approval No. SHYJS-BC-2310001). The Ethics Committee of The First Affiliated Hospital of Wenzhou Medical University waived the requirement for written informed consent for the Wenzhou cohort, and the Institutional Ethics Review Board of Shanghai Outdo Biotech waived the requirement for written informed consent for the Shanghai cohort, due to the use of anonymized leftover tissue samples obtained during routine clinical procedures. Individual informed consent was not obtained because the data were fully de-identified and the study posed no additional risk to patients. Appropriate measures were implemented to ensure patient confidentiality. No compensation was provided.

Construction and transfection of stable cell lines

Two shRNAs targeting *SMIM4* (NM_001124767.2 and NM_001308464.2) and a vector overexpressing *SMIM4* with a FLAG tag (FLAG tag: GACTACAAGGACGACGATGACAAG) at the C-terminus, along with their corresponding empty vectors, and mutant variants (Y51S, R55W, E37K, Q62P), were obtained from Tsingke Biotechnology (Beijing, China). Additionally, shRNAs targeting *SLC25A1* (NM_001256534.2), *ME1* (NM_002395.6), *ME2* (NM_001168335.2), and *GSR* (NM_000637.5) were acquired from the DNA Library of Shanghai Jiaotong University (Shanghai, China). The sequences of the shRNA-*SMIM4* (Human) were 5′-GATTTGGGAGATAAAGCTGT-3′ and 5′-GAAGCAGCGATTTGGCATCT-3′. The sequences of the shRNA-*SMIM4* (House mouse) were 5′-GCGATGTTGTACTGTCCTATT-3′ and 5′-CCTGAGATGTTCAAGATGAAA-3′. For shRNA-*SLC25A1*, the sequences were 5′-GGCTTGCAGATCCTGAAGA-3′ and 5′-AGGTTTGGAATGTTC-GAGT-3′. The shRNA-*GSR* sequence was 5′-GCATGATAAGGTACT TAGA-3′. The sequences for shRNA-*ME1* and shRNA-*ME2* were 5′-AGAGCAGTGCTACAAAATA-3′ and 5′-TGAAGAAGCATATACACTT-3′, respectively. The expression vector was co-transfected into HEK 293 T cells with two lentiviral packaging vectors, pMD2G and pSPAX2, using Lipofectamine™ 3000 reagent (Thermo Fisher Scientific). The medium containing viral particles was collected and filtered through a 0.45 μm filter (JET Biofil, Guangzhou, China) after 2 days. Stable cell lines were generated by infecting the cells with viral particles for 2 days. Infected cells were selected using 4 μg/mL puromycin (Sangon Biotech, Shanghai, China) for 2 weeks. CRISPR/Cas9-mediated *SMIM4* and *SLC25A1* knockout in PDAC cells was performed using gRNA-*SMIM4* 5′-ATCATGATTAAAGTGCGCGT-3′ and gRNA-SLC25A1 5′-CTGCGTCTTCACGTACTCGG-3′. LentiCRISPR v2 plasmid expressing the guide RNA and mCherry fluorescence protein was constructed. The mCherry fluorescence protein was used to identify the transfected cell clones. Transient depletion of *SMIM4* in MIA PaCa-2 and PANC-1 cells was achieved using the Lipofectamine™ RNAiMAX transfection reagent (Thermo Fisher Scientific) and small interfering RNA (Thermo Fisher Scientific). The siRNA sequence for *SMIM4* was 5′-GGCUGGAAGAUGAAUGA-GATT-3′.

https://doi.org/10.1038/s41467-025-64734-y

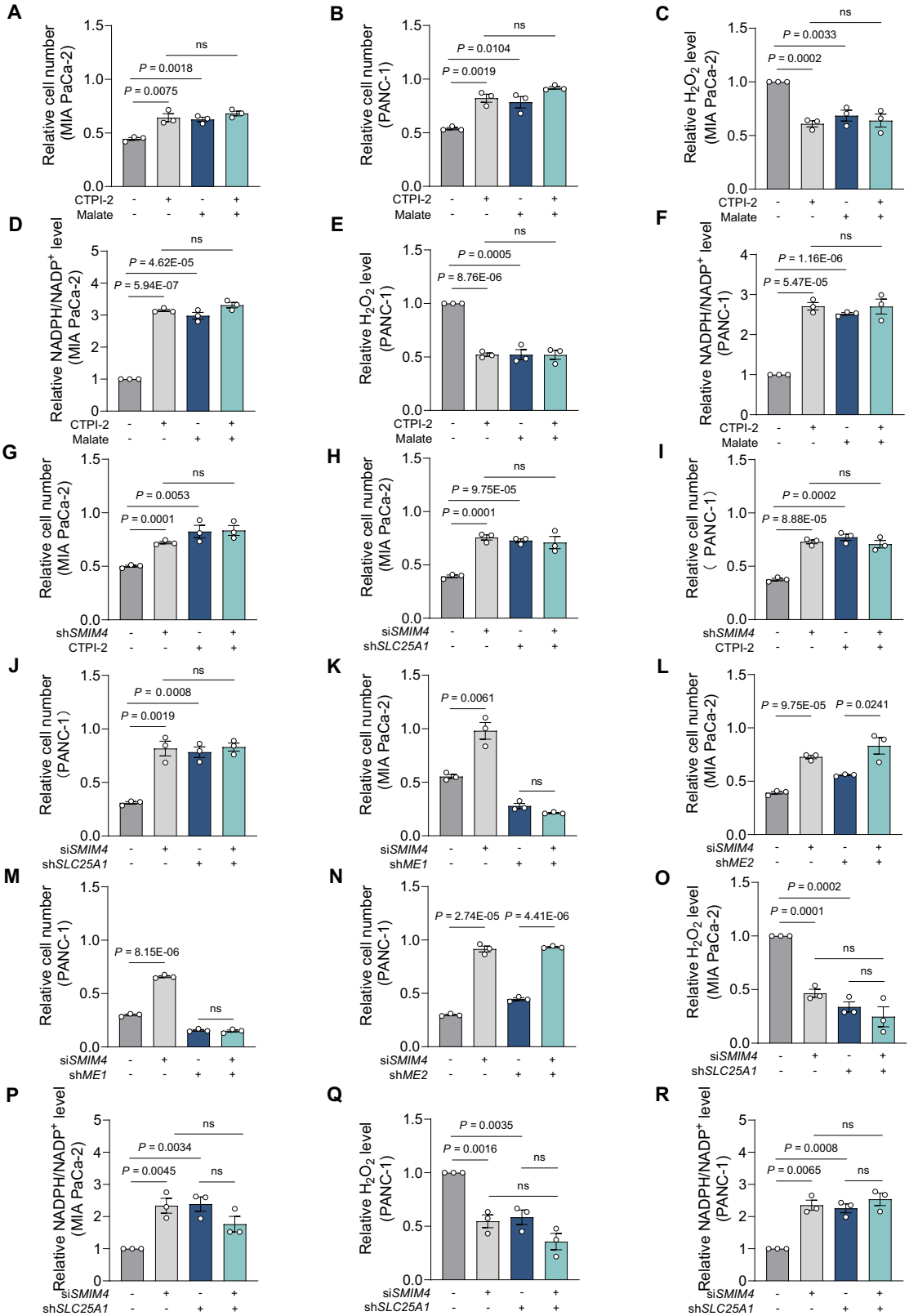

Cell lines and culture conditions

The human PDAC cell lines MIA PaCa-2, PANC-1, PaTu-8988t, CFPAC-1, BxPC3, and human HEK 293 T cells were purchased from the National Collection of Authenticated Cell Cultures (Chinese Academy of Sciences, Shanghai, China). Immortalized KPC cells were gifted by Dr. Tao Xia from Zhejiang Provincial People's Hospital. Cell authentication was conducted using short tandem repeat analysis (Genetic Testing Biotechnology Corporation, Jiangsu, China). All cells were cultured in high-glucose Dulbecco's modified Eagle's medium (DMEM, Sigma-Aldrich, Missouri, USA) containing 12% (v/v) bovine calf serum (Sigma-Aldrich), 1% (v/v) penicillin/streptomycin (Beyotime Biotechnology, Shanghai, China), and 0.25 μg/mL amphotericin B (Sangon Biotech).

Fig. 6 | *SMIM4* depletion safeguards PDAC cells from glucose deprivation induced cell death by impairing malate/citrate transporter and cytosolic malate to pyruvate conversion. A and **B** Cell number of MIA PaCa-2 (**A**) and PANC-1 (**B**) WT cells under glucose deprivation, under glucose deprivation supplemented with 10 μM CTPI-2, 4 mM malate or both 10 μM CTPI-2 and 4 mM malate for 24 h ($n = 3$ biologically independent samples). **C**–**F** H_2O_2 and NADPH/$NADP^+$ level of MIA PaCa-2 (**C**, **D**) and PANC-1 (**E**, **F**) WT cells under glucose deprivation, under glucose deprivation supplemented with 10 μM CTPI-2, 4 mM malate or both 10 μM CTPI-2 and 4 mM malate for 24 h ($n = 3$ biologically independent samples). **G** Cell number of MIA PaCa-2 cells with or without *SMIM4* depletion under glucose deprivation or under glucose deprivation supplemented with 10 μM CTPI-2 for 24 h ($n = 3$ biologically independent samples). **H** Cell number of MIA PaCa-2 cells with or without *SLC25A1* depletion, transfected with ctrl siRNA or *SMIM4* siRNA under glucose deprivation for 24 h ($n = 3$ biologically independent samples). **I** Cell number of PANC-1 cells with or without *SMIM4* depletion under glucose deprivation or under glucose deprivation supplemented with 10 μM CTPI-2 for 24 h ($n = 3$ biologically independent samples). **J** Cell number of PANC-1 cells with or without *SLC25A1* depletion, transfected with ctrl siRNA or *SMIM4* siRNA under glucose deprivation for 24 h ($n = 3$ biologically independent samples). **K**–**N** Cell number of MIA PaCa-2 (**K**, **L**) or PANC-1 (**M**, **N**) cells with or without *ME1* or *ME2* depletion, transfected with ctrl siRNA or *SMIM4* siRNA under glucose deprivation for 24 h ($n = 3$ biologically independent samples). **O**–**R** H_2O_2 and NADPH/$NADP^+$ level of MIA PaCa-2 (**O, P**) or PANC-1 (**Q, R**) cells with or without *SLC25A1* depletion, transfected with ctrl siRNA or *SMIM4* siRNA under glucose deprivation for 24 h ($n = 3$ biologically independent samples). Data are presented as means ± SEM for bar graphs from at least three independent experiments. Statistical significance was determined by unpaired two-tailed Student's *t*-test for (**A**–**R**). ns not significant. Source data are provided as a Source Data file.

For glucose or glutamine deprivation cultures, cells were cultivated using DMEM without glucose, L-glutamine, phenol red, sodium pyruvate, and sodium bicarbonate (Sigma-Aldrich) supplemented with 12% (v/v) dialyzed calf serum. For the glucose deprivation conditions, 4 mM glutamine (Sigma-Aldrich) was supplemented, while under glutamine deprivation conditions, 25 mM glucose (Sigma-Aldrich) and 1 mM sodium pyruvate (Sigma-Aldrich) were added. All cells were cultured at 37 °C in a cell culture incubator (Thermo Fisher Scientific) with 5% CO_2 and treated with 0.5 μg/mL mycoplasma removal agent (Beyotime Biotechnology).

Cell proliferation and cell survival assays

For cell proliferation and survival assays, 1×10^4 and 1×10^5 cells were plated in 12-well plates, respectively. For cell survival assays under glucose or glutamine deprivation conditions for 24 h, after overnight adherence, the cells were washed twice with phosphate-buffered saline (PBS) and replaced with deprivation medium with or without the following chemicals: N-acetyl-L-cysteine, glutathione, rotenone, antimycin A, serine, citrate, malate, L-aspartic acid dimethyl ester hydrochloride, RSL3 (Sigma-Aldrich), and CTP I-2 (MCE). After trypsinization, the cells were counted using a NovoCyte flow cytometer (Agilent, California, USA).

Blue native PAGE, SDS-PAGE, second dimension PAGE, immunoblotting, and antibodies

Blue native PAGE (BN-PAGE) was performed as described previously[94]. Briefly, proteins were lysed on ice for 20 min using 3% digitonin (Sigma-Aldrich) or 2.5% Triton ×−100 (Sigma-Aldrich), supplemented with the protease inhibitor PMSF (Sangon Biotech). The lysates were subjected to intermittent vortexing and then centrifuged at 20,000 × *g* for 20 min at 4 °C to obtain the supernatant. Protein concentration was determined using the BCA Protein Assay Kit (Beyotime Biotechnology). Mitochondrial supercomplexes and single complexes were separated using 3%–11% and 3.5%–16% gradient gels, respectively.

For SDS-PAGE, the proteins were lysed on ice for 10 min using RIPA lysis buffer (Cell Signaling Technology, Massachusetts, USA) supplemented with PMSF. The lysate was centrifuged at 14,000 × *g* for 10 min at 4 °C to obtain the supernatant.

For immunoblotting, the separated proteins were transferred onto a 0.22 μm polyvinylidene difluoride membrane (Bio-Rad, California, USA) via electroblotting. After blocking the membrane with 5% non-fat milk, the proteins were incubated overnight at 4 °C with the following primary antibodies: anti-β-Actin (sc-47778, 1:4000, Santa Cruz Biotechnology), anti-TOMM40 (18409-1-AP, 1:1000, ProteinTech), anti-SMIM4 (HPA047771, 1:4000, Sigma-Aldrich), anti-SLC25A1 (15235-1-AP, 1:4000, ProteinTech), anti-DYKDDDDK tag (66008-3-Ig, 1:1000, ProteinTech), anti-V5 tag (v5ab, 1:1000, ProteinTech), anti-UQCRC2 (ab14745, 1:1000, Abcam), anti-MTCOI (ab14705, 1:1000, Abcam), anti-TOMM20 (ab186734, 1:1000, Abcam), anti-Grim19 (ab110240, 1:1000, Abcam), anti-VDAC (4661S, 1:1000, Cell Signaling Technology), anti-HSP60 (sc-376261, 1:1000, Santa Cruz Biotechnology), anti-SDHA (ab14715, 1:2000, Abcam), anti-GRP75 (sc-133137, 1:1000, Santa Cruz Biotechnology), anti-ATP5A (ab14748, 1:1000, Abcam), anti-TOMM70 (14528-1-AP, 1:1000, ProteinTech), and anti-TIM22 (14927-1-AP, 1:1000, ProteinTech). Anti-mouse/rabbit IgG and HRP-linked antibody (7076S/7074S, 1:2000, Cell Signaling Technology) and anti-mouse/rabbit IgG and AP-linked antibody (7056S/7054S, 1:2000, Cell Signaling Technology) were used as secondary antibodies.

The anti-SMIM4 (HPA047771, Sigma-Aldrich) and anti-SLC25A1 (15235-1-AP) antibodies were locally validated by knocking out *SMIM4* and *SLC25A1* in PDAC cells, respectively. The corresponding antigen for this antibody is designated as APREST84112. Furthermore, local validation was conducted using both *SMIM4* knockout cells and tumor tissue specimens through immunohistochemical staining.

Immunohistochemistry

Paraffin-embedded tissues of human PDAC tissues were stained with anti-SMIM4 antibody (HPA047771, 1:500, Sigma-Aldrich) and anti-4-Hydroxynonenal (ab48506, 1:250, Abcam). Briefly, after deparaffinizing the sections in fresh xylene, they were hydrated with a graded ethanol series. The sections were immersed in 10 mM sodium citrate for 10 min, and this process was repeated four times for antigen retrieval. Endogenous peroxidase activity was blocked using H_2O_2. The primary antibody was added and incubated overnight at 4 °C. Then, the secondary antibody was added and incubated at room temperature for 20 min. Freshly prepared 3,3′-diaminobenzidine (DAB) substrate was added and incubated for 10 min. Subsequently, the samples were rinsed with water, stained with hematoxylin for 30 s, and dehydrated with a graded ethanol series and xylene, and then the sections were mounted. Sections were photographed with an optical microscope (Nikon Corporation, Tokyo, Japan). The use of Wenzhou cohort contains 28 patients, was approved under the ethics protocol No.2017-159 from The First Affiliated Hospital of Wenzhou Medical University, whereas the Shanghai Cohort contains 87 patients, were approved by the internal ethics review board (approval number: SHYJS-BC-2310001) from Shanghai Outdo Biotech (Shanghai, China). The average optical density (AOD) in tumor ductal cells was calculated using Image-Pro Plus 6.0 (Media Cybernetics) and reviewed by a pathologist from the Department of Pathology at The First Affiliated Hospital of Wenzhou Medical University. For survival analysis based on SMIM4 expression levels, patients were stratified using the median expression as the cutoff.

Immunofluorescence

HEK 293 T and MIA PaCa-2 cells transfected with *FLAG-SMIM4* were seeded in triplicate on coverslips (WHB, Shanghai, China) in 24-well plates. After 48 h of adhesion, cells were fixed with pre-cooled 70% ethanol at room temperature for 5 min. Then, cells were permeabilized

https://doi.org/10.1038/s41467-025-64734-y

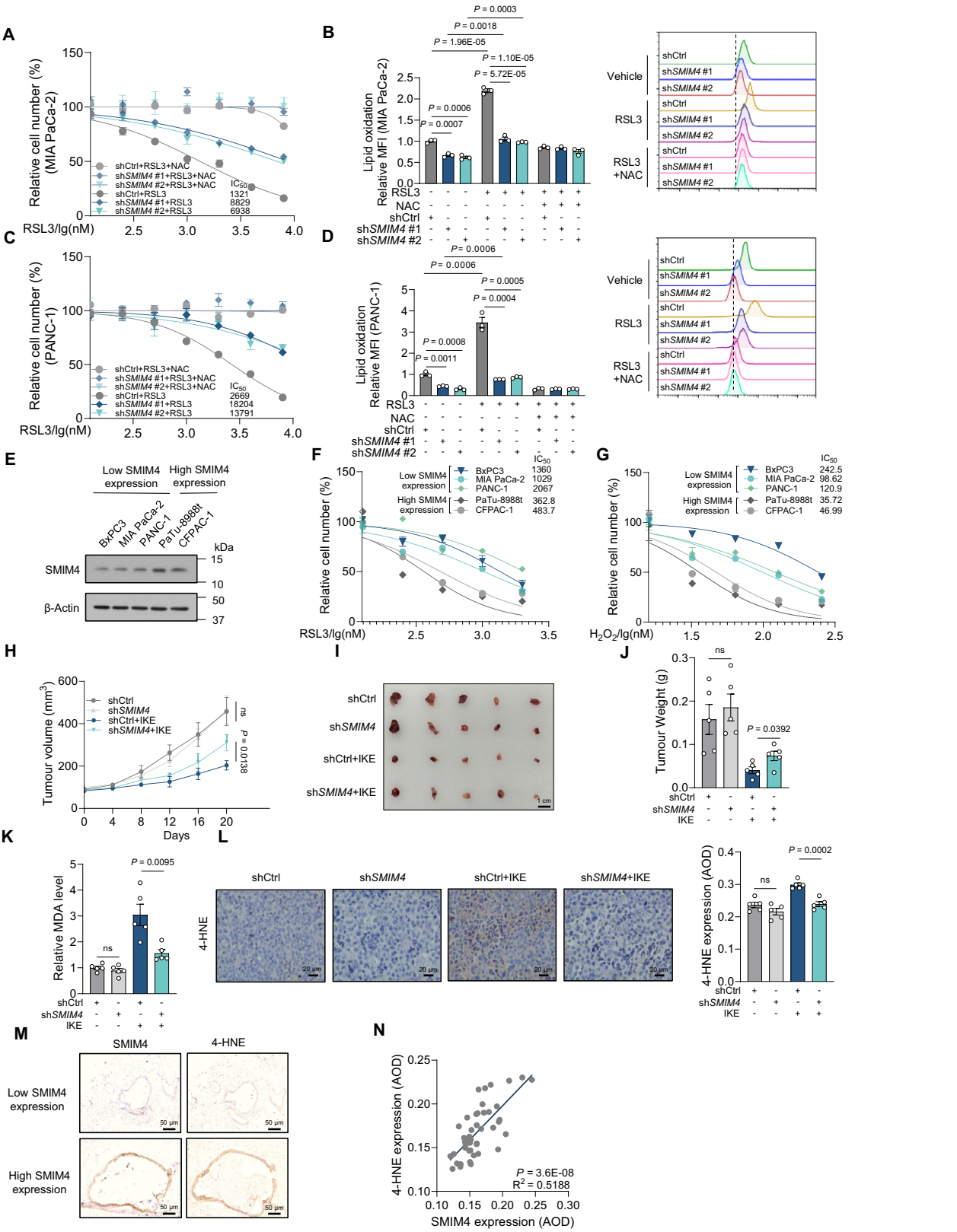

with 1.5 M HCl at room temperature for 30 min. Subsequently, cells were blocked with blocking buffer for 60 min. The primary antibodies anti-TOMM20 (ab186734, 1:250, Abcam) and monoclonal ANTI-Flag (F1804, 1:250, Sigma-Aldrich) were added and incubated overnight at 4 °C. Next, the secondary antibodies, anti-rabbit IgG-Alexa Fluor™ 488 antibody (#8878; 1:500, Cell Signaling Technology) and anti-mouse IgG-Alexa Fluor™ 594 antibody (#8890; 1:500, Cell Signaling Technology), were added and incubated at room temperature in the dark for 2 h. Then, 4 μl of mounting medium containing 4′,6-diamidino-2-phenylindole (DAPI) was added. The coverslip was mounted and the cells were observed using a confocal laser-scanning microscope (Nikon Corporation) for imaging.

Fig. 7 | Low SMIM4 expression drives resistance to lipid peroxidation and ferroptosis in vitro and in vivo. A–D Dose-dependent toxicity of RSL3 (**A** and **C**) in MIA PaCa-2 and PANC-1 cells with or without *SMIM4* depletion under glucose deprivation, with or without 40 μM NAC for 24 h ($n = 3$ biologically independent samples). Lipid peroxidation levels (**B** and **D**) in the same cells treated with 8 μM RSL3 alone or combined with 40 μM NAC for 24 h ($n = 3$ biologically independent samples). **E** Western blot analysis of SMIM4 in PDAC cell lines. Representative images are from three independent biological replicates. **F and G** Dose-dependent toxicity of RSL3 and H_2O_2 in PDAC cell lines in the absence of glucose for 24 h ($n = 3$ biologically independent samples). **H-K** Tumor growth curves (**H**) of PANC-1 xenografts with or without *SMIM4* depletion, treated with or without IKE ($n = 5$ mice). After 20 days, tumors were collected (**I**), weighed (**J**), and MDA levels measured (**K**). Scale bar: 1 cm. **L** Immunohistochemistry analyses of 4-HNE in xenografts with or without *SMIM4* depletion, treated with or without IKE for 20 days ($n = 5$ mice). Scale bar, 20 μm. **M and N** Immunohistochemistry analyses (**M**) of SMIM4 and 4-HNE in PDAC tissues ($n = 44$ pancreatic ducts per group). Pearson's correlation test was used for the correlation analysis of SMIM4 and 4-HNE expression (**N**). Scale bar: 50 μm. Data are presented as means ± SEM for bar graphs from at least three independent experiments. Statistical significance was determined by unpaired two-tailed Student's *t*-test for (**B**, **D**, **H** and **J**–**L**) and by two-sided Pearson's correlation test for (**N**). ns, not significant. Source data are provided as a Source Data file.

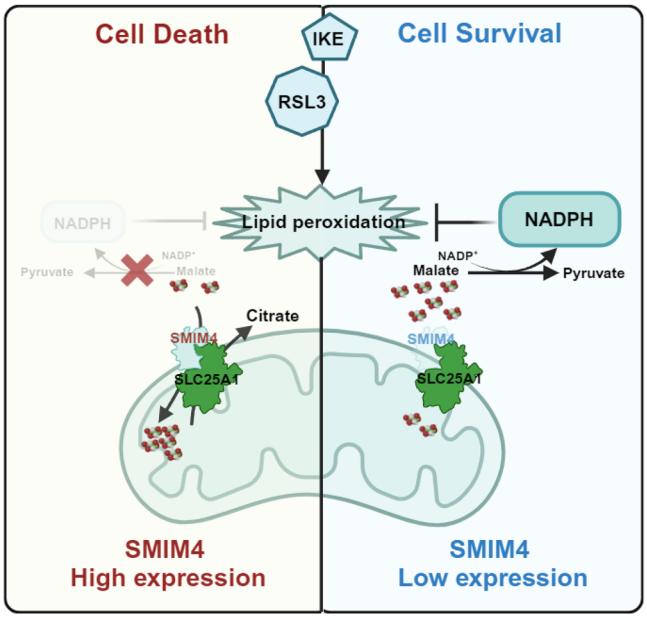

Fig. 8 | Schematic diagram depicting the mechanism of SMIM4 regulates malate transportation and lipid peroxidation resistance. Created in BioRender. Wang, B. (2025) https://BioRender.com/wpmxvaw. SMIM4 interacts with and aids SLC25A1-mediated malate/citrate transport, facilitating malate transport from the cytosol into the mitochondria. This reduction in cytosolic malate decreases NADPH production, thereby sensitizing cells to RSL3/IKE-induced lipid peroxidation and cell death (left panel). Conversely, low SMIM4 expression impairs the assembly of SLC25A1-containing complexes, resulting in altered malate compartmentalization, which boosts NADPH generation through increased cytosolic conversion of malate to pyruvate, thereby protecting cells from RSL3/IKE-induced lipid peroxidation (right panel). The image was created with BioRender.

Colony formation assay

MIA PaCa-2 and PANC-1 cells were seeded at a density of 1×10^3 cells per well in 6-well plates and cultured for 10 days. The medium was then discarded, and the cells were washed with PBS twice. Cells were then fixed with 4% paraformaldehyde for 30 min and subsequently stained with crystal violet (Beyotime Biotechnology) for 30 min. Colony numbers were counted using Image-Pro Plus 6.0 (Media Cybernetics).

Mitochondria extraction and subcellular mitochondrial localization

Mitochondria were extracted using centrifugation according to previously described methods[95]. Briefly, the cells were collected from the culture dishes using a cell scraper (Sigma-Aldrich) and washed twice with chilled PBS. The cells were homogenized in 0.1 × IB buffer (3.5 mM Tris-HCl, 2.5 mM NaCl, and 0.5 mM $MgCl_2$, pH 7.8) using a glass homogenizer (Shanghai Yuchen Biotech Co, Shanghai, China) until 70%–80% of the cells appeared blue after trypan blue staining, then 10 × IB buffer was added to revert the solution to an isotonic solution. The solution was centrifuged at 1200 × *g* and 4 °C for 3 min, and the supernatant was transferred to a new Eppendorf tube. This process was repeated until no visible pellet was observed. Finally, the supernatant was transferred to a new Eppendorf tube and centrifuged at 15,000 × *g* and 4 °C for 5 min. The supernatant was discarded and the pellet was resuspended in 1 mL of buffer A (10 mM Tris-HCl and 320 mM sucrose, pH 7.40). The sample was re-centrifuged at 15,000 × *g*, 4 °C for 5 min and the supernatant was discarded, the resulting pellet was the crude mitochondrial fraction. For the carbonate extraction experiment, isolated mitochondria were treated with sodium carbonate (0.1 M Na_2CO_3, pH 11.5, Sigma-Aldrich) on ice for 30 min. Subsequently, PMSF was added, and the mixture was centrifuged at 75,000 × *g* for 1 h using an ultracentrifuge (Beckman Coulter, California, USA). The proteins were detected using western blotting. TOMM20 (an outer mitochondrial membrane protein) and HSP60 (mitochondrial matrix protein) were used as markers. To localize the proteins within the mitochondria, isolated mitochondria were treated with or without 1 mg/mL proteinase K (Sigma-Aldrich) and 20% Triton X-100 (Sigma-Aldrich) on ice for 30 min, followed by the addition of PMSF. TIM22 (inner mitochondrial membrane protein), HSP60 (mitochondrial matrix protein), and TOMM20 (outer mitochondrial membrane protein) were used as markers.

Mice

Four-week-old male nude mice from Zhejiang Vital River Experimental Animal Technology Co., Ltd. (Zhejiang, China) were subcutaneously injected with PANC-1 cells (5.0×10^6) with or without *SMIM4* depletion. Tumor size was measured using an electronic caliper every 5 days and calculated using the formula: 0.5 × length × width^2. For IKE treatment, when the tumor volume reached an average of 100 mm^3, mice were randomly assigned to treatment groups and intraperitoneally (IP) administered 23 mg/kg IKE every 2 days for 20 days[96]. For the KPC genetically engineered mouse-derived orthotopic allografts (GDA) mouse model, KPC cells were orthotopically injected at a density of 1.0×10^6 mouse PDAC cells in 50 μL of Matrigel (354248, Corning) into the pancreas of eight-week-old male syngeneic immunocompetent C57BL/6 mice, which were purchased from GemPharmatech Co., Ltd. (Jiangsu, China)[67]. The mice study was performed under the protocol (No. wydw2022-0589) approved by laboratory animal ethics committee of Wenzhou Medical University. The maximal tumor volume allowed is 1000 mm^3, and we confirm that this limit was not exceeded in any of the experiments. Mice were housed in a specific pathogen-free facility under controlled conditions with a 12-h light/dark cycle, ambient temperature maintained at 21–23 °C, and 50% relative humidity. Standard rodent diet and autoclaved water were provided ad libitum.

Co-immunoprecipitation and mass spectrometry

Co-IP experiments were performed using the Pierce Crosslink Magnetic IP/Co-IP Kit (Thermo Fisher Scientific) according to the manufacturer's instructions. Briefly, mitochondria were isolated from cells and solubilized in lysis buffer (25 mM Tris, 150 mM NaCl, 0.5% NP-40, 1 mM EDTA-Na_2, 5% glycerol, pH 7.4) for 30 min at 4 °C. After centrifugation at 14,000 × *g* for 10 min, the supernatant was incubated

overnight at 4 °C with rotation with either Pierce™ Protein A/G Magnetic Beads (Thermo Fisher Scientific) conjugated with anti-SLC25A1 antibody, anti-SMIM4 antibody, or control rabbit IgG, all crosslinked to the beads using DSS, or with Pierce™ Anti-DYKDDDDK Magnetic Agarose (Thermo Fisher Scientific). The bound complexes were eluted using the elution buffer, neutralized, and analyzed by LC-MS/MS (Jingjie PTM BioLab Co., Ltd., Hangzhou, China; Shanghai Applied Protein Technology, Shanghai, China) or standard immunoblotting.

GST pull-down assay

The recombinant proteins GST-SMIM4 (in pGEX-4T-2) and His-SLC25A1-IS (in ET32a(+)) were expressed in Escherichia coli BL21(DE3) and purified using Glutathione Sepharose™ 4B beads (Cytiva, Massachusetts, USA) and Ni-NTA Agarose beads (QIAGEN, Hilden, Germany), respectively. For the GST pull-down assay, GST Beads were incubated with the recombinant proteins. GST alone was used as a negative control. Protein interactions were analyzed by immunoblotting using GST-Tag(12G8) mAb and His-Tag(2A8) Antibody (Abmart, Shanghai, China).

OXPHOS complex enzyme activity assay

Enzyme activity for Complex I–V were assessed in isolated mitochondria as described in our previous published works[33,97]. Assay buffers for Complex I–V were freshly and were pre-warmed at 37 °C for 10 min. Crude mitochondria were added and the Complex I–V related reaction were monitored using a multifunctional plate reader (SpectraMax iD3, Molecular Devices, Silicon Valley, USA). Enzyme activity for each complex was normalized to the activity of complex II.

Measurement of mitochondrial-dependent respiration

The mitochondrial respiration rate was determined using an Oxygraph-2k (Oroboros, Innsbruck, Austria) following previously established protocols[98]. Following previously established protocols, 5×10^6 cells were permeabilized with 0.02 mg/mL digitonin (Sigma-Aldrich). After recording the baseline data, CI- and CII-dependent respiration were measured by adding respiratory substrates: 6 mM of both malate and glutamate (Sigma-Aldrich) for CI, and 4 mM succinate (Sigma-Aldrich) for CII. Additionally, 0.1 μM rotenone (Sigma-Aldrich) and 1 mg/mL 3-nitropropionic acid (Sigma-Aldrich) were used as inhibitors. Cell numbers were counted using a NovoCyte flow cytometer before being permeabilized with 0.02 mg/mL digitonin for normalized respiration data.

Quantitative polymerase chain reaction

In accordance with the manufacturer's instructions, RNA was extracted using TRIzol reagent (Thermo Fisher Scientific) and reverse transcribed using a reverse transcription kit (Takara Biotechnology, Kyoto, Japan), respectively. Subsequently, quantitative polymerase chain reaction (qPCR) was performed using fluorogenic SYBR Green dye (Bio-Rad). The amplification primer sequences are listed in Supplementary Table 1. The qPCR was performed using Quantagene q225 real-time PCR system (Kubo Tech, Beijing, China) and data were analyzed using the relative quantification method ($2^{-\Delta\Delta CT}$)[99].

Flow cytometric detection of ROS, lipid peroxidation, apoptosis, and cell cycle

For ROS and lipid peroxidation detection, the samples were measured in 1 mL of pre-warmed PBS (5% FBS), and Bodipy-C11 (Thermo Fisher Scientific) or H2DCFDA (Thermo Fisher Scientific) were added to a final concentration of 5 μM. The samples were incubated with the dye at 37 °C in the dark for 30 min and washed twice with PBS. The signal in the FITC channel was measured.

For apoptosis detection, the samples were measured using the FITC Annexin V Apoptosis Detection Kit I (BD Biosciences, California, USA). After washing twice with PBS, cells were resuspended in 1× binding buffer at a concentration of 1×10^6 cells/ml. Then, 100 μl of the solution containing 1×10^5 cells was transferred to a new Eppendorf tube, and 5 μl of FITC Annexin V and 5 μl of propidium iodide (PI) were added. The cells were gently vortexed and incubated for 15 min at room temperature in the dark. Finally, 400 μl of 1 × binding buffer was added, and the sample was analyzed using flow cytometry after 1 h.

Cell cycle analysis was performed using PI/RNase staining buffer (BD Biosciences). Cells were collected and fixed in cold 70% ethanol (pre-cooled overnight) at −20 °C for 4 h. Next, 1×10^6 cells were washed once with PBS and incubated with 0.5 mL of PI/RNase staining buffer for 15 min at room temperature. The samples were analyzed using flow cytometry within 1 h.

Measurement of GSH/GSSG ratio, $NADP^+$/NADPH ratio, and H_2O_2 level

Measurements of the GSH/GSSG ratio were conducted using a GSH and GSSG Assay Kit (Beyotime Biotechnology) in accordance with the manufacturer's instructions. Briefly, samples were subjected to two rapid freeze-thaw cycles using liquid nitrogen and a 37 °C water bath. Subsequently, the samples were centrifuged at 10,000 × *g*, 4 °C for 10 min to collect the supernatant for analysis. The absorbance was measured at 412 nm using multifunctional plate reader (SpectraMax iD3).

Measurements of the $NADP^+$/NADPH ratio were conducted using the $NADP^+$/NADPH Assay Kit (Beyotime Biotechnology) in accordance with the manufacturer's instructions. Briefly, cells were lysed by adding 1×10^6 cells to 200 μl of $NADP^+$/NADPH extraction buffer. The supernatant was collected for analysis after centrifugation at 2000 × *g* at 4 °C for 10 min. The absorbance was measured at 450 nm using multifunctional plate reader (SpectraMax iD3).

Measurements of the H_2O_2 level were conducted using a Hydrogen peroxide assay kit (Beyotime Biotechnology) in accordance with the manufacturer's instructions. Briefly, add 1×10^6 cells to 200 μl of hydrogen peroxide detection lysis buffer for cell lysis. Centrifuge at approximately 12,000 × *g* at 4 °C for 5 min, then collect the supernatant for subsequent analysis. The absorbance was measured at 560 nm using multifunctional plate reader (SpectraMax iD3).

Electron microscopy

Following previously established protocols[100], cells were fixed with 2.5% glutaraldehyde and 1% Osmium tetroxide, pre-stained with 1% uranyl acetate, and dehydrated stepwise using gradient acetone. After embedding, the samples were sectioned and examined using transmission electron microscopy (Hitachi, Ltd., Tokyo, Japan).

Metabolomic analysis

Metabolite profiling was performed according to the protocol provided by Calibra Scientific Inc. (Key Laboratory of Digital Technology of Zhejiang Province, China). Briefly, cells were trypsinized, washed twice with ice-cold PBS, and 1×10^7 cells were snap-frozen in liquid nitrogen for 30 min prior to analysis.

Glutamine- and glucose-derived metabolic flux

Stable isotope tracing experiments with [U-^{13}C] glucose and [U-^{13}C] glutamine (Cambridge Isotope Laboratories, Massachusetts, USA) were performed using DMEM powder (Sigma-Aldrich) supplemented with 12% (v/v) dialyzed calf serum. Glutamine- and glucose-derived metabolic flux were measured according to previously described methods[58]. Cells were washed twice with PBS, and the medium was replaced with 20 mM [U-^{13}C] glucose- or 2 mM [U-^{13}C] glutamine-containing labeled medium and incubated for 6 h. After incubation, the process was terminated, and cells were washed twice with pre-cooled PBS. The cells were digested with trypsin and washed twice with PBS and the cell pellet was collected. The samples were snap-frozen in liquid nitrogen for 30 min. Samples were sent to Metabo-Profile (Shanghai, China) for metabolic flux assay.

Malate uptake assay

Malate uptake of isolated mitochondria was conducted as previously described [33, 82]. Briefly, 200 μg of isolated mitochondria were resuspended in 200 μl incubation buffer (1 mM ethylene glycol tetraacetic acid, 10 mM NaCl, 2 mM KH_2PO4, 2 mM $MgCl_2$, 10 mM 3-(N-morpholino) propanesulfonic Acid, 125 mM KCl, pH 7.2) in a 1.5 ml Eppendorf tube, supplemented with 200 μl reaction buffer (2 mM ADP, 4 mM KH_2PO_4, 0.25 M KCl, 4 mM $MgCl_2$, 4 mM ethylene glycol tetraacetic acid, 4% bovine serum albumin, 40 mM Tris-HCl, 0.5 mM pyruvate sodium, 1 mM [U-^{13}C] malate, pH 7.4). The mixture was incubated in a water bath for 20 min at 37 °C. Subsequently, the tube was placed on ice for 30 s. The mitochondria washed twice with 500 μl pre-cooled 1× KPBS (136 mM KCl, 10 mM KH_2PO4, pH 7.25) and centrifugation at 15,000 × *g* at 4 °C for 2 min. The samples were snap-frozen in liquid nitrogen for 30 min and then stored at −80 °C. Samples were assayed by Shanghai ProfLeader Biotech Co. (Shanghai, China).

Measurement of cellular and cytosolic malate levels

Measurement of cellular and cytosolic malate levels was performed using the Malate Assay Kit (Sigma-Aldrich) in accordance with the manufacturer's instructions. Briefly, after washing the cells twice with PBS, they were resuspended in malate assay buffer at a concentration of 5×10^6 cells/ml. Following three cycles of freezing and thawing in liquid nitrogen, the samples were passed through a 10 kDa MWCO spin filter (Beyotime Biotechnology) and then incubated with detection buffers for 30 min. The absorbance was measured at 412 nm. For the measurement of cytosolic malate levels, 1×10^6 cells were lysed with 0.1 × IB buffer and then restored with 10 × IB buffer. The lysate was centrifuged at 1200 × *g* at 4 °C for 3 min, and the supernatant was transferred to a new Eppendorf tube. This process was repeated until no visible pellet was observed. Finally, the sample was centrifuged at 15,000 × *g* at 4 °C for 5 min to collect the supernatant. Detection buffers were added to assay the cytosolic malate level.

Measurement of serine levels

For the measurement of cellular serine levels, cells were digested using trypsin, washed twice with pre-cooled PBS, and snap-frozen in liquid nitrogen. A total of 1×10^7 cells were processed and analyzed by Calibra Diagnostics (Hangzhou, China). The samples were separated using a CalQuant-S HPLC system equipped with a C18 column (Phenomenex, 100 × 2.1 mm, 2.6 μm) and quantified using a CalQuant-S mass spectrometer in MRM mode. Raw data were processed with MultiQuant 3.0.3 software to extract peak areas for serine and the internal standard. Serine concentrations were calculated based on the ratio of serine peak area to internal standard peak area and determined using a standard curve.

Bioinformatic analyses

RNA expression and clinical data related to *SMIM4* expression in pancreatic cancer and normal pancreatic tissues were downloaded from the TCGA (https://portal.gdc.cancer.gov) and GTEx (https://gtexportal.org) databases and the GSE28735 dataset (https://www.ncbi.nlm.nih.gov/geo/). KEGG-based GSEA was performed using the Bioinformatics cloud platform (https://www.bioinformatics.com.cn/) to identify statistically significant differences in pathways.

Molecular docking

A molecular docking simulation was performed to model potential interactions between SMIM4 and SLC25A1 using the protein-protein docking webserver HADDOCK. Structures of SMIM4 (Q8WVI0) and SLC25A1 (P53007) were downloaded from the AlphaFold Protein Structure Database (AlphaFoldDB, https://alphafold.ebi.ac.uk/). Figure 5F was generated using PyMOL (Schrödinger, Oregon, USA).

The amino acid mutation types at the predicted binding site and their corresponding ΔΔGbind (kcal/mol) were predicted using MutBind2 (https://lilab.jysw.suda.edu.cn/research/mutabind2/). The MutaBind2 model uses molecular mechanics force fields, statistical potentials and fast side-chain optimization algorithms built via random forest (RF) method.

Dialysis serum

A serum dialysis protocol was employed to process 300 mL of serum. Initially, a 10× dialysis buffer (5 L) was prepared by dissolving 151.425 × *g* Tris-base, 37.275 × *g* KCl, and 400.314 × *g* NaCl in 5 L of ultrapure water, followed by pH adjustment to 7.35 with approximately 90 mL HCl. The serum, previously thawed at 4 °C for two days and thoroughly mixed, was placed into pre-cut dialysis tubing (MWCO:1000 kDa) under UV-sterilized conditions within a biosafety cabinet. The tubing was secured to a 15 mL pipette positioned above a 5 L beaker, and serum was transferred into the tubing using a 50 mL centrifuge tube. Both ends of the tubing were promptly clamped to prevent drying. The tubing was then submerged in 5 L of dialysis buffer (prepared by diluting 500 mL of the 10× buffer with ultrapure water to a final volume of 5 L) and dialyzed at 4 °C with continuous stirring using a magnetic stirrer. The dialysis buffer was replaced every hour for a total of 10 cycles, followed by a 2-h incubation after the ninth exchange and overnight dialysis after the final exchange. The following day, the dialyzed serum was transferred into 50 mL centrifuge tubes (not exceeding 40 mL per tube) within the biosafety cabinet, and glucose levels were confirmed to be low using test strips. The serum was then labeled, stored at −30 °C, and filtered through a 0.22 μm filter before use.

Statistics & reproducibility

Data are presented as means ± SEM from at least three independent replicates. Unless otherwise specified, statistical analysis was conducted using an unpaired two-tailed Student's *t*-test to compare results between two groups. Pearson's correlation test was used for correlation analysis. The log-rank test was performed to analyze survival results, which were expressed as Kaplan–Meier survival curves. IF and IHC images represent randomly selected images from biological samples. For in vivo studies, mice were randomly assigned to different experimental groups. No statistical methods were used to predetermine sample sizes, however, based on our previous experimental experience, we used enough samples to achieve statistically significant results. No data were excluded from analyses. Statistical analysis and data visualization were performed using Prism 10.0 (GraphPad Software, California, USA). A p-value of <0.05 was considered statistically significant. Detailed methods are described in each individual figure legend.

Reporting summary

Further information on research design is available in the Nature Portfolio Reporting Summary linked to this article.

Data availability

The metabolomics data generated in this study have been deposited in the National Genomics Data Center database under accession code PRJCA043295. The previously published RNA-seq data used in this study, that were reanalyzed here are available in the GEO database under accession numbers GSE28735. Transcriptomic and clinical data from the TCGA-PAAD project were downloaded from the Genomic Data Commons (GDC) portal (https://portal.gdc.cancer.gov/projects/TCGA-PAAD). All other data supporting the findings of this study are available within the Article, Supplementary Information, or Source Data files. Source data are provided with this paper.

References

1. Siegel, R. L., Miller, K. D., Wagle, N. S. & Jemal, A. Cancer statistics, 2023. *CA Cancer J. Clin.* **73**, 17–48 (2023).

2. Neoptolemos, J. P., Springfeld, C. & Hackert, T. A review of pancreatic cancer. *JAMA* **326**, 2436 (2021).
3. Sherman, M. H. & Beatty, G. L. Tumor microenvironment in pancreatic cancer pathogenesis and therapeutic resistance. *Annu. Rev. Pathol.* **18**, 123–148 (2023).
4. Kamphorst, J. J. et al. Human pancreatic cancer tumors are nutrient poor and tumor cells actively scavenge extracellular protein. *Cancer Res.* **75**, 544–553 (2015).
5. Sullivan, M. R. et al. Quantification of microenvironmental metabolites in murine cancers reveals determinants of tumor nutrient availability. *Elife* **8**, e44235 (2019).
6. Davidson, S. M. et al. Direct evidence for cancer-cell-autonomous extracellular protein catabolism in pancreatic tumors. *Nat. Med.* **23**, 235–241 (2017).
7. Banh, R. S. et al. Neurons release serine to support mRNA translation in pancreatic cancer. *Cell* **183**, 1202–1218.e1225 (2020).
8. Sousa, C. M. et al. Pancreatic stellate cells support tumour metabolism through autophagic alanine secretion. *Nature* **536**, 479–483 (2016).
9. Li, Z. et al. Cancer cells depend on environmental lipids for proliferation when electron acceptors are limited. *Nat. Metab.* **4**, 711–723 (2022).
10. Nwosu, Z. C. et al. Uridine-derived ribose fuels glucose-restricted pancreatic cancer. *Nature* **618**, 151–158 (2023).
11. Skinner, O. S. et al. Salvage of ribose from uridine or RNA supports glycolysis in nutrient-limited conditions. *Nat. Metab.* **5**, 765–776 (2023).
12. Parker, S. J. et al. Selective alanine transporter utilization creates a targetable metabolic niche in pancreatic cancer. *Cancer Discov.* **10**, 1018–1037 (2020).
13. Mukhopadhyay, S. et al. Autophagy is required for proper cysteine homeostasis in pancreatic cancer through regulation of SLC7A11. *Proc. Natl. Acad. Sci. USA* **118**, e2021475118 (2021).
14. Warburg, O. On the origin of cancer cells. *Science* **123**, 309–314 (1956).
15. Birsoy, K. et al. An essential role of the mitochondrial electron transport chain in cell proliferation is to enable aspartate synthesis. *Cell* **162**, 540–551 (2015).
16. Sullivan, L. B. et al. Supporting aspartate biosynthesis is an essential function of respiration in proliferating cells. *Cell* **162**, 552–563 (2015).
17. Martinez-Reyes, I. et al. Mitochondrial ubiquinol oxidation is necessary for tumour growth. *Nature* **585**, 288–292 (2020).
18. Schild, T. et al. NADK is activated by oncogenic signaling to sustain pancreatic ductal adenocarcinoma. *Cell Rep.* **35**, 109238 (2021).
19. Ren, X. et al. The Fe-S cluster assembly protein IscU2 increases alpha-ketoglutarate catabolism and DNA 5mC to promote tumor growth. *Cell Discov.* **9**, 76 (2023).
20. Nie, K. et al. COX6B2 drives metabolic reprogramming toward oxidative phosphorylation to promote metastasis in pancreatic ductal cancer cells. *Oncogenesis* **9**, 51 (2020).
21. Chandel, N. S. NADPH-the forgotten reducing equivalent. *Cold Spring Harb. Perspect. Biol.* **13**, a040550 (2021).
22. Vaziri-Gohar, A. et al. Limited nutrient availability in the tumor microenvironment renders pancreatic tumors sensitive to allosteric IDH1 inhibitors. *Nat. Cancer* **3**, 852–865 (2022).
23. Son, J. et al. Glutamine supports pancreatic cancer growth through a KRAS-regulated metabolic pathway. *Nature* **496**, 101–105 (2013).
24. Rensvold, J. W. et al. Defining mitochondrial protein functions through deep multiomic profiling. *Nature* **606**, 382–388 (2022).
25. Banh, R. S. et al. The polar oxy-metabolome reveals the 4-hydroxymandelate CoQ10 synthesis pathway. *Nature* **597**, 420–425 (2021).
26. Papalazarou, V. et al. Phenotypic profiling of solute carriers characterizes serine transport in cancer. *Nat. Metab.* **5**, 2148–2168 (2023).
27. Wang, Y. et al. SLC25A39 is necessary for mitochondrial glutathione import in mammalian cells. *Nature* **599**, 136–140 (2021).
28. Yoo, H. C. et al. A variant of SLC1A5 is a mitochondrial glutamine transporter for metabolic reprogramming in cancer cells. *Cell Metab.* **31**, 267–283.e212 (2020).
29. Kunji, E. R. S., King, M. S., Ruprecht, J. J. & Thangaratnarajah, C. The SLC25 carrier family: important transport proteins in mitochondrial physiology and pathology. *Physiol. (Bethesda)* **35**, 302–327 (2020).
30. Hewton, K. G., Johal, A. S. & Parker, S. J. Transporters at the interface between cytosolic and mitochondrial amino acid metabolism. *Metabolites* **11**, 112 (2021).
31. Cunningham, C. N. & Rutter, J. 20,000 picometers under the OMM: diving into the vastness of mitochondrial metabolite transport. *EMBO Rep.* **21**, e50071 (2020).
32. Kory, N. et al. SFXN1 is a mitochondrial serine transporter required for one-carbon metabolism. *Science* **362**, eaat9528 (2018).
33. Fang, H. et al. SERAC1 is a component of the mitochondrial serine transporter complex required for the maintenance of mitochondrial DNA. *Sci. Transl. Med.* **14**, eabl6992 (2022).
34. Shi, X. et al. Combinatorial GxGxE CRISPR screen identifies SLC25A39 in mitochondrial glutathione transport linking iron homeostasis to OXPHOS. *Nat. Commun.* **13**, 2483 (2022).
35. Chen, Y. J. et al. An integrated bioinformatic investigation of mitochondrial solute carrier family 25 (SLC25) in colon cancer followed by preliminary validation of member 5 (SLC25A5) in tumorigenesis. *Cell Death Dis.* **13**, 237 (2022).
36. Luongo, T. S. et al. SLC25A51 is a mammalian mitochondrial NAD(+) transporter. *Nature* **588**, 174–179 (2020).
37. Zhang, G. et al. Integration of metabolomics and transcriptomics revealed a fatty acid network exerting growth inhibitory effects in human pancreatic cancer. *Clin. Cancer Res.* **19**, 4983–4993 (2013).
38. Thul, P. J. et al. A subcellular map of the human proteome. *Science* **356**, eaal3321 (2017).
39. Mottis, A., Herzig, S. & Auwerx, J. Mitocellular communication: shaping health and disease. *Science* **366**, 827–832 (2019).
40. Kanda, T. et al. Heterogeneity of metabolic adaptive capacity affects the prognosis among pancreatic ductal adenocarcinomas. *J. Gastroenterol.* **57**, 798–811 (2022).
41. Dennerlein, S. et al. Defining the interactome of the human mitochondrial ribosome identifies SMIM4 and TMEM223 as respiratory chain assembly factors. *Elife* **10**, e68213 (2021).
42. Podmanicky, O. et al. Mitochondrial aminoacyl-tRNA synthetases trigger unique compensatory mechanisms in neurons. *Hum. Mol. Genet.* **33**, 435–447 (2024).
43. Ho, W. J., Jaffee, E. M. & Zheng, L. The tumour microenvironment in pancreatic cancer - clinical challenges and opportunities. *Nat. Rev. Clin. Oncol.* **17**, 527–540 (2020).
44. Grünwald, B. T. et al. Spatially confined sub-tumor microenvironments in pancreatic cancer. *Cell* **184**, 5577–5592.e5518 (2021).
45. Wang, B. et al. ROS-induced lipid peroxidation modulates cell death outcome: mechanisms behind apoptosis, autophagy, and ferroptosis. *Arch. Toxicol.* **97**, 1439–1451 (2023).
46. Gago-Dominguez, M., Jiang, X. & Castelao, J. E. Lipid peroxidation, oxidative stress genes and dietary factors in breast cancer protection: a hypothesis. *Breast Cancer Res.* **9**, 201 (2007).
47. Elkin, E. R., Harris, S. M. & Loch-Caruso, R. Trichloroethylene metabolite S-(1,2-dichlorovinyl)-l-cysteine induces lipid peroxidation-associated apoptosis via the intrinsic and extrinsic

apoptosis pathways in a first-trimester placental cell line. *Toxicol. Appl. Pharm.* **338**, 30–42 (2018).
48. Yao, W., Maitra, A. & Ying, H. Recent insights into the biology of pancreatic cancer. *EBioMedicine* **53**, 102655 (2020).
49. Encarnación-Rosado, J. et al. Targeting pancreatic cancer metabolic dependencies through glutamine antagonism. *Nat. Cancer.* **5**, 85–99 (2023).
50. Bott, A. J. et al. Glutamine anabolism plays a critical role in pancreatic cancer by coupling carbon and nitrogen metabolism. *Cell Rep.* **29**, 1287–1298.e1286 (2019).
51. Fang, X. et al. Malic enzyme 1 as a novel anti-ferroptotic regulator in hepatic ischemia/reperfusion injury. *Adv. Sci. (Weinh.)* **10**, e2205436 (2023).
52. Yang, H. et al. SIRT3-dependent GOT2 acetylation status affects the malate-aspartate NADH shuttle activity and pancreatic tumor growth. *Embo J.* **34**, 1110–1125 (2015).
53. Broeks, M. H. et al. The malate-aspartate shuttle is important for de novo serine biosynthesis. *Cell Rep.* **42**, 113043 (2023).
54. Ruprecht, J. J. & Kunji, E. R. S. The SLC25 mitochondrial carrier family: structure and mechanism. *Trends Biochem. Sci.* **45**, 244–258 (2020).
55. Nah, J. et al. Microprotein SMIM26 drives oxidative metabolism via serine-responsive mitochondrial translation. *Mol. Cell.* **85**, 2759–2775.e12 (2025).
56. van Zundert, G. C. P. et al. The HADDOCK2.2 web server: user-friendly integrative modeling of biomolecular complexes. *J. Mol. Biol.* **428**, 720–725 (2016).
57. Zhang, N. et al. MutaBind2: predicting the impacts of single and multiple mutations on protein-protein interactions. *iScience* **23**, 100939 (2020).
58. Arnold, P. K. et al. A non-canonical tricarboxylic acid cycle underlies cellular identity. *Nature* **603**, 477–481 (2022).
59. Li, Y. et al. Blockage of citrate export prevents TCA cycle fragmentation via Irg1 inactivation. *Cell Rep.* **38**, 110391 (2022).
60. Korge, P., Calmettes, G. & Weiss, J. N. Reactive oxygen species production in cardiac mitochondria after complex I inhibition: modulation by substrate-dependent regulation of the NADH/NAD(+) ratio. *Free Radic. Biol. Med.* **96**, 22–33 (2016).
61. Li, S. et al. Nicotinamide nucleotide transhydrogenase-mediated redox homeostasis promotes tumor growth and metastasis in gastric cancer. *Redox Biol.* **18**, 246–255 (2018).
62. Zhang, R. et al. Oncogenic KRASG12D reprograms lipid metabolism by upregulating SLC25A1 to drive pancreatic tumorigenesis. *Cancer Res.* **83**, 3739–3752 (2023).
63. Tan, M. et al. Inhibition of the mitochondrial citrate carrier, Slc25a1, reverts steatosis, glucose intolerance, and inflammation in preclinical models of NAFLD/NASH. *Cell Death Differ.* **27**, 2143–2157 (2020).
64. Fernandez-Fuente, G., Rigby, M. J. & Puglielli, L. Intracellular Citrate/acetyl-CoA flux and endoplasmic reticulum acetylation: connectivity is the answer. *Mol. Metab.* **67**, 101653 (2023).
65. Ding, C. C. et al. MESH1 is a cytosolic NADPH phosphatase that regulates ferroptosis. *Nat. Metab.* **2**, 270–277 (2020).
66. Nguyen, K. T. et al. The MARCHF6 E3 ubiquitin ligase acts as an NADPH sensor for the regulation of ferroptosis. *Nat. Cell Biol.* **24**, 1239–1251 (2022).
67. Koikawa, K. et al. Targeting Pin1 renders pancreatic cancer eradicable by synergizing with immunochemotherapy. *Cell* **184**, 4753–4771.e4727 (2021).
68. Ju, H. Q., Lin, J. F., Tian, T., Xie, D. & Xu, R. H. NADPH homeostasis in cancer: functions, mechanisms and therapeutic implications. *Signal Transduct. Target Ther.* **5**, 231 (2020).
69. Liu, Y. H., Hu, C. M., Hsu, Y. S. & Lee, W. H. Interplays of glucose metabolism and KRAS mutation in pancreatic ductal adenocarcinoma. *Cell Death Dis.* **13**, 817 (2022).
70. Halbrook, C. J. & Lyssiotis, C. A. Employing metabolism to improve the diagnosis and treatment of pancreatic cancer. *Cancer Cell* **31**, 5–19 (2017).
71. Wang, Y. P. et al. Arginine methylation of MDH1 by CARM1 inhibits glutamine metabolism and suppresses pancreatic cancer. *Mol. Cell* **64**, 673–687 (2016).
72. Zarei, M. et al. Posttranscriptional upregulation of IDH1 by HuR establishes a powerful survival phenotype in pancreatic cancer cells. *Cancer Res.* **77**, 4460–4471 (2017).
73. Hall, I. H. et al. Role of thiol agents in protecting against the toxicity of helenalin in tumor-bearing mice. *Planta Med.* **55**, 513–517 (1989).
74. Busch, J. D. et al. MitoRibo-tag mice provide a tool for in vivo studies of mitoribosome composition. *Cell Rep.* **29**, 1728–1738 e1729 (2019).
75. Liang, C. et al. Mitochondrial microproteins link metabolic cues to respiratory chain biogenesis. *Cell Rep.* **40**, 111204 (2022).
76. Bottani, E. et al. TTC19 plays a husbandry role on uqcrfs1 turnover in the biogenesis of mitochondrial respiratory complex III. *Mol. Cell* **67**, 96–105 e104 (2017).
77. Tamai, S. et al. Characterization of the mitochondrial protein LETM1, which maintains the mitochondrial tubular shapes and interacts with the AAA-ATPase BCS1L. *J. Cell Sci.* **121**, 2588–2600 (2008).
78. Wang, Y. et al. Knockdown of BRAWNIN minimally affect mitochondrial complex III assembly in human cells. *Biochim. Biophys. Acta Mol. Cell Res.* **1871**, 119601 (2024).
79. He, M. et al. A new genetic disorder in mitochondrial fatty acid beta-oxidation: ACAD9 deficiency. *Am. J. Hum. Genet.* **81**, 87–103 (2007).
80. Cimadamore-Werthein, C. et al. Human mitochondrial carriers of the SLC25 family function as monomers exchanging substrates with a ping-pong kinetic mechanism. *EMBO J.* **43**, 3450–3465 (2024).
81. Capobianco, L., Ferramosca, A. & Zara, V. The mitochondrial tricarboxylate carrier of silver eel: dimeric structure and cytosolic exposure of both N- and C-termini. *J. Protein Chem.* **21**, 515–521 (2002).
82. Liu, Y. et al. Autoregulatory control of mitochondrial glutathione homeostasis. *Science* **382**, 820–828 (2023).
83. Shi, X. et al. Dual regulation of SLC25A39 by AFG3L2 and iron controls mitochondrial glutathione homeostasis. *Mol. Cell* **84**, 802–810.e806 (2024).
84. Pareek, V., Sha, Z., He, J., Wingreen, N. S. & Benkovic, S. J. Metabolic channeling: predictions, deductions, and evidence. *Mol. Cell* **81**, 3775–3785 (2021).
85. Fernandez, H. R. et al. The mitochondrial citrate carrier, SLC25A1, drives stemness and therapy resistance in non-small cell lung cancer. *Cell Death Differ.* **25**, 1239–1258 (2018).
86. Jin, E. S., Lee, M. H., Murphy, R. E. & Malloy, C. R. Pentose phosphate pathway activity parallels lipogenesis but not antioxidant processes in rat liver. *Am. J. Physiol. Endocrinol. Metab.* **314**, E543–E551 (2018).
87. Ohanele, C. et al. The mitochondrial citrate carrier SLC25A1 regulates metabolic reprogramming and morphogenesis in the developing heart. *Commun. Biol.* **7**, 1422 (2024).
88. Palmieri, E. M. et al. Nitric oxide orchestrates metabolic rewiring in M1 macrophages by targeting aconitase 2 and pyruvate dehydrogenase. *Nat. Commun.* **11**, 698 (2020).
89. Hertz, L., Yu, A. C. & Schousboe, A. Uptake and metabolism of malate in neurons and astrocytes in primary cultures. *J. Neurosci. Res.* **33**, 289–296 (1992).
90. Liu, X., Zhang, Y., Zhuang, L., Olszewski, K. & Gan, B. NADPH debt drives redox bankruptcy: SLC7A11/xCT-mediated cystine uptake as a double-edged sword in cellular redox regulation. *Genes Dis.* **8**, 731–745 (2021).

91. Liu, L. et al. Malic enzyme tracers reveal hypoxia-induced switch in adipocyte NADPH pathway usage. *Nat. Chem. Biol.* **12**, 345–352 (2016).
92. Song, X. et al. PDK4 dictates metabolic resistance to ferroptosis by suppressing pyruvate oxidation and fatty acid synthesis. *Cell Rep.* **34**, 108767 (2021).
93. Lim, J. S., Kim, E., Song, J. S. & Ahn, S. Energy-stress-mediated activation of AMPK sensitizes MPS1 kinase inhibition in triple-negative breast cancer. *Oncol. Rep.* **52**, 101 (2024).
94. Wittig, I., Braun, H. P. & Schägger, H. Blue native PAGE. *Nat. Protoc.* **1**, 418–428 (2006).
95. Zhou, D. et al. Protocol for mitochondrial isolation and sub-cellular localization assay for mitochondrial proteins. *STAR Protoc.* **4**, 102088 (2023).
96. Zhang, Y. et al. Imidazole ketone erastin induces ferroptosis and slows tumor growth in a mouse lymphoma model. *Cell Chem. Biol.* **26**, 623–633.e629 (2019).
97. Spinazzi, M., Casarin, A., Pertegato, V., Salviati, L. & Angelini, C. Assessment of mitochondrial respiratory chain enzymatic activities on tissues and cultured cells. *Nat. Protoc.* **7**, 1235–1246 (2012).
98. Fang, H. et al. A membrane arm of mitochondrial complex I sufficient to promote respirasome formation. *Cell Rep.* **35**, 108963 (2021).
99. Livak, K. J. & Schmittgen, T. D. Analysis of relative gene expression data using real-time quantitative PCR and the 2(-Delta Delta C(T)) method. *Methods* **25**, 402–408 (2001).
100. Zhang, K. et al. Mitochondrial supercomplex assembly regulates metabolic features and glutamine dependency in mammalian cells. *Theranostics* **13**, 3165–3187 (2023).

Acknowledgements

We thank the members of our lab for vector construction, and the Scientific Research Center of Wenzhou Medical University for consultation and access to instruments that supported this work. We also thank The First Affiliated Hospital of Wenzhou Medical University and Shanghai Outdo Biotech for providing tissue samples and associated data. This work was supported by grants from the National Natural Science Foundation of China—Excellent Young Scientists Fund (No. 82222043 to H.F), the "Pioneer" and "Leading Goose" R&D Program of Zhejiang Province (No. 2024C03152 to H.F.), Zhejiang Provincial Natural Science Foundation of China (Grant No. LRG25H200001 to H.F), the National Natural Science Foundation of China (No. 82172322 to H.F., No. 82272435 to W.C., No. 82372303 to M.J.), the Non-profit Central Research Institute Fund of Chinese Academy of Medical Sciences (2024-RC320-01 to H.F.), and Joint Funds of the National Natural Science Foundation of China (U22A20342 to J.L.).

Author contributions

H.F., J.L. (Jianxin Lyu), W.C., and M.J. conceived and designed the study. B.W., X.H., X.L., J.W., C.Y., K.C., Y.C., F.M., H.J., F.Z., Y.Z., J.L. (Jinya Lyu), Y.B., X.Q., and D.Z. performed the experiments. H.F., B.W., X.H., X.L., and J.W. drafted the paper. B.W., X.H., and X.L. analyzed and finalized the data. All authors read and approved the paper.

Competing interests

The authors declare no competing interests.

Additional information

Supplementary information The online version contains supplementary material available at https://doi.org/10.1038/s41467-025-64734-y.

Correspondence and requests for materials should be addressed to Minghua Jiang, Wei Cui, Jianxin Lyu or Hezhi Fang.

Peer review information *Nature Communications* thanks the anonymous reviewer(s) for their contribution to the peer review of this work. A peer review file is available.